Summer 8-4-2011

Pulsed Laser Deposition of Thin Film Heterostructures

Ezra Garza
University of New Orleans, epgarza@my.uno.edu

Pulsed Laser Deposition of Thin Film Heterostructures

A Thesis

Submitted to the Graduate Faculty of the
University of New Orleans
in partial fulfillment of the
requirements for the degree of

Master of Science
in
Applied Physics

by

Ezra Garza

B.S. University of New Orleans, 2008

August, 2011

Acknowledgments

I would like to thank Dr. Leonard Spinu for giving me the opportunity of being a part of such a great research group and guidance during the research process. Thank you to Dr. Leszek Malkinski, Dr. Kevin Stokes, and Dr. Gabriel Caruntu, my thesis committee members for their time. Also, thanks to Dr. Gabriel Caruntu and his research group for supplying the PTO samples and assistance in various measurements. My special thanks goes to the all the amazing, great, and inspiring professors of the physics department. This work was supported by the Department of Defense through the ARO under Grant No. W911NF-08-C0131, Louisiana Board of Regents Contract #LEQSF(2007-12)-ENH-PKSFI-PRS-04, as well as the Advanced Materials Research Institute (AMRI) at the University of New Orleans.

Table of Contents

List of Figures vi

List of Tables viii

Abstract ix

Chapter 1: Introduction 1

1.1 Overview 1

1.2 Thesis Organization 2

Chapter 2: PLD Equipment 3

2.1 Introduction 3

2.2 The Laser 4

2.3 PLD Optics 6

2.3.1 Lenses 7

2.3.2 Mirrors and Beam Splitters 8

2.3.3 Deposition Chamber Windows 9

2.4 The Deposition System 10

2.4.1 Deposition Chamber 11

2.4.2 Vacuum Pumps 11

2.4.3 Gas Flow and Monitoring Pressure 12

2.4.4 Target and Substrate Holders 13

Chapter 3: Mechanisms and Thin Film Formation 15

3.1 Introduction 15

3.2 Laser-Target Interaction 16

3.2.1 Ablation Threshold 17

3.2.2 Ablation/Sputtering Mechanisms 20

3.3 Plasma Plume Formation 22

3.4 Nucleation and Growth of Thin Films 24

Chapter 4: Pulsed Laser Deposition of Strontium Ruthenate Thin Films. 27

4.1 Introduction 27

4.2 Applications for Sr_2RuO_4 28

4.3 Experimental Procedure 29

4.4 Results and Discussion 33

4.5 Conclusion 38

Chapter 5: Pulsed Laser Deposition of Terfenol-D Thin Films 40

5.1 Introduction 40

5.2 Applications for Terfenol-D 41

5.3 Experimental Procedure 42

5.4 Results and Discussion 45

5.5 Conclusion 57

Chapter 6: General Conclusion 58

References 60

Appendix A 65

Vita 68

List of Figures

Figure 2.1. A general PLD system configuration 3

Figure 3.1. Shadowgraph of plume at 1200ps 23

Figure 3.2. Growth Modes: (a) Frank-Van der Merwe; (b) Volmer-Weber; (c) Stranski-Krastanov 25

Figure 4.1. Sr_2RuO_4 Layered Perovskite Crystal Structure 28

Figure 4.2. FESEM of Sr_2RuO_4 Target Surface 33

Figure 4.3. θ-2θ XRD scan of Sr_2RuO_4 Target 34

Figure 4.4. θ-2θ XRD scan of STO and LAO substrates 34

Figure 4.5. θ-2θ XRD scan of S_2RO_4/STO thin film 35

Figure 4.6. θ-2θ XRD scan of S_2RO_4/LAO thin film.....36

Figure 4.7. Resistance Measurement for Sr_2RuO_4/STO.....37

Figure 4.8. Resistance Measurement for Sr_2RuO_4/LAO 37

Figure 4.9. FESEM of S_2RO_4/STO Surface.....38

Figure 4.10. FESEM of S_2RO_4/LAO Surface 38

Figure 5.1. FESEM of TD Target.....46

Figure 5.2. θ-2θ XRD scan of TD Target 46

Figure 5.3. θ-2θ XRD scan of 280nm PTO 47

Figure 5.4. Cross-sectional FESEM (a) and Topography AFM (b) images of $PbTiO_3$ layer 48

Figure 5.5. Heterostructure Nanocomposite 49

Figure 5.6. VSM Hysteresis of TD250/PTO275 49

Figure 5.7. θ-2θ XRD scan of TD250/PTO275 50
Figure 5.8. AFM and MFM images of TD250/PTO275.....51
Figure 5.9. Phase Hysteresis Loops of TD250/PTO275 51
Figure 5.10. Piezoelectric amplitude signal of TD250/PTO275.....52
Figure 5.11. θ-2θ XRD scan of TD39/PTO280 53
Figure 5.12. θ-2θ XRD scan of TD204/PTO280 54
Figure 5.13. θ-2θ XRD scan of TD327/PTO280 54
Figure 5.14. AFM images of Annealed Samples.....54
Figure 5.15. Phase Hysteresis Loops of Annealed Samples.....56
Figure 5.16. Piezoelectric amplitude signal of Annealed Samples 57
Figure A.1. Labeled XRD Scan of Sr_2RuO_4 Target 65
Figure A.2. AGM of TD39/PTO280 65
Figure A.3. AGM Expanded View of TD39/PTO280.....65
Figure A.4. AGM of TD204/PTO280 66
Figure A.5. AGM Expanded View of TD204/PTO280 66
Figure A.6. AGM of TD327/PTO280 66
Figure A.7. AGM Expanded View of TD327/PTO280 67

List of Tables

Table 2.1. Performance parameters: Excimer versus Nd:YAG laser systems 5

Table 2.2. Parameters: LOTIS TII LS-2147 Nd:YAG Laser System..... 6

Table 2.3. Transmittance Range of Common Optical Materials..... 8

Table 4.1. EDS measurement of Sr_2RuO_4 Target.....33

Table 5.1. EDS measurement of Terfenol-D Target 46

Table 5.2. Amplitude vs. Bias Voltage Data for Annealed Samples 55

Table 5.3. Piezoelectric Coefficients for Annealed Samples.....55

ABSTRACT

Thin films of Strontium Ruthenate have been grown on Strontium Titanate and Lanthanum Aluminate (100) substrates by pulsed laser deposition. X-ray diffraction results show that the films grown on the Strontium Titanate are amorphous and polycrystalline on the Lanthanum Aluminate. Resistances versus temperature measurements show that the films exhibit semiconducting characteristics. In addition to the growth of Strontium Ruthenate thin films, multilayer heterostructures of Terfenol-D thin films on polycrystalline Lead Titanate thin films were grown by pulsed laser deposition. By using a novel experimental technique called magnetic field assisted piezoelectric force microscopy it is possible to investigate the magnetoelectric coupling between the electrostrictive Lead Titanate and magnetostrictive Terfenol-D thin film. Upon examination of the produced thin films the phase and amplitude components of the piezoelectric signal experience changes in response to an applied in-plane magnetic field. These changes provide experimental evidence of a magnetoelectric coupling between the Terfenol-D and Lead Titanate layers.

Strontium Ruthenate, amorphous, polycrystalline, semiconducting characteristics, heterostructures, Terfenol-D, Lead Titanate, magnetoelectric coupling

Chapter 1: Introduction

1.1 Overview

Pulsed laser deposition (PLD) has been used for growing thins films since the mid 1960's. In 1965, Smith and Turner were the first to use a pulsed laser to deposit thin films. They successfully deposited films with a ruby laser onto multiple substrates such as semiconductors and dielectrics.[1]

Laser and target material interaction govern the PLD the process. High-energy laser pulses interact with the target material and the target material is removed by vaporization. The vaporization produces a plasma plume of particles that condense on a substrate to produce a thin film. The laser ablation technique is what makes PLD attractive for thin film deposition, because the ablation of the target preserves its stoichiometry in the thin film. The PLD process is simple and versatile, these characteristics have made it possible to successfully deposit high quality thin films of various materials such as oxides, high-temperature superconductors, magnetoelectrics, and ceramics to list a few.

The focus of this research is to use PLD to deposit functional thin film heterostructures. Specifically, two types of thin films will be investigated; Strontium Ruthenate (Sr_2RuO_4) and Terfenol-D ($Tb_{.3}Dy_{.7}Fe_{1.92}$). For the Sr_2RuO_4 thin films, the motivation was to achieve superconductivity to aid in

the development of new applications for superconducting electronics and semiconductor technology. The Terfenol-D thin films were produced to investigate the magnetoelectric effect (ME) between the magnetostrictive Terfenol-D and an adjoining coupled Lead Titanate piezoelectric layer.

1.2 Thesis Organization

Chapter 2 will have information on the PLD equipment. The mechanisms of PLD and thin film formation will be discussed in chapter 3. Chapter 4 will have material information, applications, the experimental procedure, results and discussion, and conclusion for the growth of Sr_2RuO_4 thin films. The same will be explained in chapter 5 for the Terfenol-D thin films. Chapter 6 will be a general conclusion for all the work done in this thesis, followed by references, appendices, and vita.

Chapter 2: PLD Equipment

2.1 Introduction

This chapter will present the technical attributes of the pulsed laser deposition (PLD) system used for this thesis research and give a general guide for the type of equipment required for PLD. The PLD technique is versatile in the fabrication of numerous types of thin films, and just as versatile is the PLD system. A PLD system can be assembled piece by piece, or purchased complete as a ready to use system. This is one advantage of PLD, the ability for the user to build and assemble a system for their desired specifications or have a prepackaged system assembled for them. As for the PLD system, it is quite simple. Though there are many parts which make up a complete PLD system each has its own specific purpose.

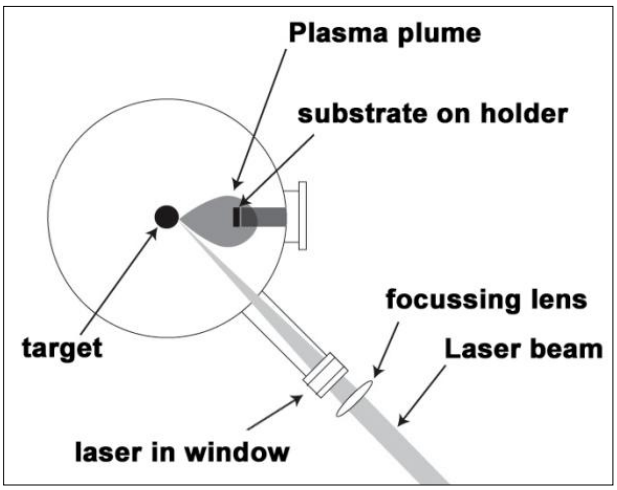

Figure 2.1. A general PLD system configuration.

2.2 The Laser

As the name suggests, pulsed laser deposition uses a pulsed laser. There are many reasons for the use of a pulsed laser though the main reason is that a pulsed laser can easily achieve the energies required for a material to transform into plasma. Of equal importance is the lasers operating wavelength; thin film growth can be done at various wavelengths but when considering a laser for PLD most thin film growth is done between 200nm and 400nm laser wavelengths. The primary purpose for using these wavelengths are because the majority of the materials used for PLD have strong absorption in these ranges.[2]

To date the most accomplished work has been done with pulsed laser systems that operate in the ultraviolet (UV) range, specifically nanosecond excimer and neodymium-doped yttrium aluminum garnet (Nd^{3+}: YAG or Nd:YAG) pulsed lasers.[2] Excimer lasers are a type of gas laser and get there name from the lasing process, energy is pumped into a gaseous lasing medium mixture that give rise to excimer molecules. These molecules undergo spontaneous emission and aid in stimulated emission of photons in the UV wavelengths.

The Strontium Ruthenate (Sr_2RuO_4) and Terfenol-D ($Tb_{.3}Dy_{.7}Fe_{1.92}$) thin films for this research were produced by the LOTIS TII LS-2147 Nd:YAG laser system. The Nd:YAG is a solid-state system, and uses the neodymium-doped yttrium aluminum garnet crystal as the lasing medium. Flash lamps in

the lasers housing excite the Nd in the YAG crystal, a Q-switch allows the gain medium to reach the maximum population inversion and when reached the lasing process begins. Nd:YAG lasers have a fundamental laser emission of 1064nm, in order to achieve other wavelengths nonlinear optics are used to frequency double to 532nm. The 532nm output is the mixed with residual 1064nm or frequency doubled to achieve the desired 355nm and 266nm wavelengths for PLD.[2]

Table 2.1. Performance parameters: Excimer versus Nd:YAG laser systems

Parameter	***Excimer System***	***Nd:YAG System***
Wavelength (nanometers)	248 nm	266 nm
Output Energy (millijoules)	100 - 1200 mJ	40 - 200 mJ
Repetition Rate (Hertz)	Variable, 1 - 200 Hz	Fixed, 1 - 30 Hz
Shot-to-Shot Stability (root mean square)	0.5 - 1%, rms	8 - 12%, rms
Long Term Drift, 4 hours (root mean square)	0 - 1%, rms	10 - 15%, rms

Sources: [2, 3]

Table 1.1. has performance parameters for current excimer and Nd:YAG systems at the 248 nm and 266 nm wavelengths respectively because these

wavelengths are the most popular for PLD. Table 1.2. has the parameters for the LOTIS TII LS-2147 Nd:YAG laser system.

Table 2.2. Parameters: LOTIS TII LS-2147 Nd:YAG Laser System

Parameter	***Value***
Wavelength (nanometers)	1064, 532, 355, 266 nm
Pulse Energy FF, SH at 10Hz (millijoules)	869mJ; 420mJ
TH, FH	188mJ; 113mJ
Pulse Repetition Rates (Hertz)	1, 2, 5, 10 Hz
Pulse Duration at FWHM FH (nanoseconds)	14-15 ns

Source: [4]

2.3 PLD Optics

In a PLD system following the pulsed laser system is the optics, Figure 2.1 shows a focusing lens and a deposition chamber window; this is the optical setup for our PLD system, it is the simplest configuration and assures the least amount of laser energy loss between the laser and target material.

Another simple way to assure the least amount of laser energy loss is to keep optics clean. This will also prevent damage of optical components. Additional components are need for more elaborate PLD systems, such as:

- Mirrors
- Beam Splitters
- Apertures

The following sections will discuss the purpose of each component.

2.3.1 Lenses

With any system that incorporates optics, lenses are going to constituent a major role in system design. For PLD, lenses focus the laser light and control the laser fluence. The most common lens used in PLD is the spherical lens this is because it magnifies in two planes and the projected laser energy is oriented as a point. Cylindrical lenses are also used but only magnify in one plane, hence the projected image will be a line. A fused silica plano-convex lens made by CVI Melles Griot with a focal length of 772mm is the main lens used in our system.

In order to choose the correct lens for your PLD system, consider your operating wavelength, laser beam size and energy when it passes through the lens. The type of material the lens is composed of will determine if the lens has the characteristics that are need for your system. Considering the

size of the lens is essential, the lens should be at least 1.5 times the $1/e^2$ Gaussian laser beam diameter so that 99% of the beam passes through the lens.[2] Lastly, the damage threshold of the lens needs to be considered so that the lens is not damaged during the PLD process. High laser fluence on the magnitude at or exceeding 10 J/cm^2 is needed for some materials, so one needs to make sure that the laser energy at the lens is below the damage threshold. Table 1.3. gives the transmittance range of common optical materials used in PLD.

Table 2.3. Transmittance Range of Common Optical Materials

Material	*Transmittance Range (nm)*
Calcium Fluoride (CaF_2)	150 – 8000
Magnesium Fluoride (MgF_2)	130 – 8000
Sapphire	150 – 5000
UV Fused Silica	190 - 2500, 2600 – 4000

Sources: [2, 5]

2.3.2 Mirrors and Beam Splitters

Mirrors and beam splitters allow a PLD system to contain multiple deposition chambers. These components allow redirection of the laser beam to multiple chambers for different PLD experiments, they also make it

possible for the user to perform dual beam PLD in a single chamber. As with all optics, mirrors and beam splitters have operating parameters. Again great consideration needs to be taken when choosing mirrors and beam splitters for your PLD system.

Operating wavelength, laser energy, and reflectance-transmittance ratios are important when selecting mirrors and beam splitters. The wavelength is important because mirrors have optimum reflectance performance at specified wavelengths and beam splitters have reflectance-transmittance ratios that govern the intensity of the laser beam after it is split. As with the lenses, mirrors and beam splitters have damage thresholds; so consider this parameter when selecting these components. Keep in mind that when designing a multiple chamber PLD systems try to place the mirrors and beam splitters before a focusing lens. This will decrease the probability of damage to both the mirror and beam splitter.

2.3.3 Deposition Chamber Windows

The chamber windows are the simplest optical component of the PLD system. Multiple window ports can be located on a deposition chamber; our chamber has two view windows and one laser window. A chamber used for dual beam PLD will have two laser windows. View windows are used to observe the plasma plume and aid in target alignment with the laser beam. They can be made of various materials such as optical glass or crystal

quartz. Usually when selecting the right view window the requirements are the ability for you to see through them, handle the stress associated with high vacuum, and a high enough operating temperature to tolerate the radiate heat from the substrate heater. The laser window needs to meet the same requirements as well as others. Laser windows should have a high degree of flatness, and be polished. Including the above requirements, select the laser window with consideration to operating wavelength, transmittance ability, and damage threshold. Also proper alignment of the laser beam with the laser window is at 0º incidence, this will prevent any additional optical aberrations. The view and laser window characteristics for our system are as follows:

PLD View and Laser Windows used our system

- Crystal Quartz: two view windows
- Sapphire: laser window

2.4 The Deposition System

When referring to the deposition system this includes the chamber and all components attached to the chamber. Think of the deposition chamber as the central hub, when combined with vacuum pumps, gauges, gas flow, target and substrate holders it becomes the deposition system and the quality of your system will ultimately determine your ability to successfully deposit films. As with the laser and optics, the user must select the right deposition system for their PLD applications. Deposition systems are

commercially available and purchasing such a system is probably the easiest way to go when assembling a PLD system. Although, these commercial systems tend to be more costly then assembling a deposition system piece by piece.

2.4.1 Deposition Chamber

Deposition chambers are an essential piece of the PLD system; concerning chamber requirements for PLD, the chamber should have high vacuum capabilities, additional inlets for new components, and be large enough to vary the target and substrate distance. The chamber used for this research has a cylindrical geometry and a volume of approximately .134m^3. It is capable of high vacuum and uses conflat (CF) flanges and feed-throughs, the use of copper gaskets insure a leak tight fit. The chamber also has additional inlets for new components if desired and a gate valve on the bottom that is used to open and close the chamber when pulling vacuum.

2.4.2 Vacuum Pumps

A turbomolecular and rotary vane pump allow the deposition chamber to achieve high vacuum. The two pumps work as one unit, the vane pump is used as a backing pump to bring the chamber pressure below 10^{-2} Torr and then the turbomolecular pump (TMP) is switched on to achieve high vacuum conditions. TMPs are high speed and need a backing pump to operate

because most are unable to operate at pressures higher than 10^{-2} Torr by design. If the pressures exceed 10^{-2} Torr the TMP blades will be subjected to high strains, this will cause the blades to slow, the pump will become inefficient, and damage could occur. An Alcatel Adixen 2015SD Pascal Series dual stage rotary vane is used as our backing pump and the water cooled Oerlikon Leybold TurboVac 600C is the TMP. A Leybold Heraeus TurboTronik NT 20 controls the TurboVac 600C. When at full operational capacities our chamber with this two-pump configuration, can sustain pressures between 4 X 10^{-7} and 9 X 10^{-7} Torr during thin film deposition that does not require background gas flow.

2.4.3 Gas Flow and Monitoring Pressure

As with other physical vapor deposition systems (PVD), a background gas may be needed to grow certain thins films in PLD. There are many options on how to control the gas flow into the chamber. With our system, a single inlet allows a background gas to be introduced for deposition. A stainless steel Swagelok low-flow metering 1/4 inch valve with a vernier handle regulates this gas flow. Another way to regulate gas flow would be to use a mass flow controller in combination with a mass flow controller power supply equip with a gas flow readout, more recently mass flow controllers integrated with module controls and digital readouts have eliminated the use for an external power supply/readout. To monitor chamber pressure during

PLD the use of a gauge controller with a high and low pressure gauge is common practice. To measure pressures from 760 to 10^{-3} Torr a Kurt J. Lesker (KJL) convection gauge is used; below 10^{-3} Torr to 10^{-9} Torr, a KJL ion gauge monitors pressure; the controller readout is a KJL 6600 series.

2.4.4 Target and Substrate Holders

Most target holders for PLD are a carousel design; this design has multiple holder stages that can rotate in and out of the lasers path. This design enables the deposition of multilayer films without having to open the deposition chamber between the deposition of layers. The current holder for our deposition chamber is a feed-through carousel design with 6 holders for 25 millimeter diameter and 6 millimeter thick targets. A copper water-cooled shield protects the other five targets when they are not being used from cross contamination, and substrate heater radiation; this shield also provides protection for the target holder's mechanisms from the plasma plume.

Directly across from the target holder is the substrate holder, it is positioned so that the plasma plume and substrate are on the same axis. The substrate holder is adjustable to vary the target and substrate distance. A platinum heater supplies a maximum substrate temperature of 1000°C. A McAllister Technical Services programmable temperature controller with a K-type thermocouple is used for temperature control and monitoring. Two

independent McAllister Technical Services target and substrate control modules control the target and substrate rotation during thin film deposition.

Chapter 3: PLD Mechanisms and Thin Film Formation

3.1 Introduction

The pulsed laser deposition (PLD) technique to grow thin films was introduced in the mid 1960's by Smith and Turner. Though successful, the technique was not widely accepted until the 1980's; by then laser technology had progressed. In 1983 Cheung was the first to grow an epitaxial film that was comparable in quality to the leading deposition technique at the time molecular beam epitaxy (MBE).[6] After the successful deposition of the high-temperature superconductor yttrium barium copper oxide (YBaCuO) by Dijkkamp in 1987, interest in thin film growth by PLD became a high pursued technique.[7]

Ablation, the process that expels material from the target preserves the stoichiometry during the PLD process. In return, the produced thin films attain characteristics of the target material, from mechanical to magnetic properties. As simple as the PLD method is, some complications can be present. Surface modification of the target material, caused by laser irradiation and can lead to thin films having large particulates on the surface. These particulates can halter epitaxial growth where desired and change the morphology of the thin film surface.

The deposition of thin films from start to finish can be categorized into three stages:

- Laser-Target Interaction
- Plasma Plume Formation
- Nucleation and Growth of Thin Films

3.2 Laser-Target Interaction

The laser-target interaction is the driving mechanism of the PLD process. Through the years, theoretical models and experimental studies have been formulated in the attempt to explain the processes that govern the PLD ablation process. These studies have shown that the ablation process is not governed by a single mechanism but by multiple mechanisms that arise due to the laser-target interaction. When the laser pulse is incident on the target, absorption of the laser energy gives way to target ablation; ablation is the sputtering/mass removal of the target material.

In order for the target material to be ablated the absorbed laser pulse energy must be greater than the binding energy of an atom to the surface which is the energy of vaporization per atom, $E_{ab} > E_b$.[8] The energy of the laser pulse is first absorbed by the electrons; this causes them to oscillate and become excited. The exited electrons transfer their energy to the material lattice through electron-phonon interactions; this transfer of energy takes place over a picosecond time scale and is noted by, $t_{e\text{-}L}$, the

temperature equilibration time and a electron heat conduction with a characteristic time t_{th}.[8] Current laser technology has the capability of producing laser pulses that are less than the relaxation times, $t_p < (t_{e\text{-}L} + t_{th})$. If the laser pulse is less than these times, then the ablation process is non-thermal and if the relaxation times are less than the pulse-width, the ablation process is thermal. The LOTIS TII LS-2147 Nd:YAG laser system is a nanosecond laser, so we will focus on the thermal ablation process. Additional information on the mechanisms of ultrafast pulse laser ablation can be found in [8] and multiple papers [9-11].

3.2.1 Ablation Thresholds

The ablation threshold is the amount of energy needed for the ablation process to begin. In PLD this energy is expressed as *(F)* the laser fluence in (joules/cm^2):

$$F = I\left(t_p\right) \tag{3.1}$$

where *(I)* is the laser intensity (watts/cm^2) and (t_p) is the laser pulse width duration (seconds). The ablation threshold for dielectrics and metals vary greatly because the fluence is dependent on laser parameters and material characteristics.

Parameters that influence ablation thresholds

- Laser pulse width, and wavelength
- Target material's electromagnetic, and thermal properties

To gain an understanding on how these parameters will vary the ablation threshold, we will start by discussing the skin depth. The skin depth in meters for a material can be expressed as:

$$\delta \equiv \frac{1}{\kappa} \tag{3.2}$$

(κ) is the imaginary part of

$$K = k + i\kappa \tag{3.3}$$

which is a result from the solutions when the curl is applied to Maxwell's equations;

$$\nabla X \boldsymbol{E} = -\frac{\partial \boldsymbol{B}}{\partial t} \tag{3.4}$$

$$\nabla X \boldsymbol{B} = \mu\epsilon \frac{\partial \boldsymbol{E}}{\partial t} + \mu\sigma \boldsymbol{E} \tag{3.5}$$

(k) is the wave number, *(μ)* the permeability (Newton/Ampere^2), (ϵ) the permittivity (Farad/meter), and *(σ)* represents the conductivity of the material (Siemens/meter).

One of the variables that the skin depth is dependent on is the wavelength of the laser. This is apparent in the equation for skin depth:

$$\kappa \equiv \omega \sqrt{\frac{\epsilon\mu}{2}} \left[\sqrt{1 + (\frac{\sigma}{\epsilon\omega})^2} - 1 \right]^{1/2} \tag{3.6}$$

where *(ω)* is the angular frequency (radians/second) of the laser light. Incorporating the skin depth with the thermal diffusion coefficient (α):

$$\frac{\delta^2}{\alpha} \approx t_{heat} \tag{3.7}$$

the result is approximately the electron heat conduction time t_{heat} in seconds, this is the time for the electron temperature to smooth across the skin depth.[12] The equation for the thermal diffusion coefficient (meters^2/second) is:

$$\alpha = \frac{k}{C_p \rho} \tag{3.8}$$

here (k) is the thermal conductivity (Watts/Kelvin-meter), *(C_p)* the specific heat capacity (Joules/Kelvin), and *(ρ)* the material density (kilograms/meter^3). To formulate an equation for fluence the absorption coefficient *(A)* of the material must also be known, this is given by [13].

$$A \equiv 2\kappa \tag{3.9}$$

Together with the binding energy of vaporization per atom *(E_b)*, and the number density of atoms in the material *(n_a)* the following equation can approximate the fluence threshold for laser pulse durations that are larger than 10 picoseconds: [12]

$$F_{th} \approx \frac{(\alpha\, t_p)^{1/2}\, E_b\, n_a}{A} \tag{3.10}$$

An example of this approximation is given in [12] for copper where: E_b = 3.125eV/atom, n_a = .845 X 10^{23} cm^{-3}, A = 1, α = 1.14 cm^2/s. These parameters give an approximation:

$$F_{th} = .045\, X\, (t_p[ps])^{1/2} \tag{3.11}$$

3.2.2 Ablation/Sputtering Mechanisms

When the fluence threshold for the target material is reached ablation/sputtering will begin. The primary mechanisms in nano-pulse PLD are:

- Thermal sputtering
- Electronic sputtering
- Exfoliational sputtering
- Hydrodynamic sputtering

As stated earlier ablation is only possible when the absorbed laser pulse energy is greater than energy of vaporization per atom, $E_{ab} > E_b$. After

this criterion is met if the relaxation times are less than the pulse width $t_p > (t_{e\text{-}L} + t_{th})$, the ablation is thermal. Thermal sputtering follows this model in that the absorbed laser energy is high enough to cause vaporization of the target material. Electronic sputtering is normally confined to dielectrics and wide band-gap semiconductors, it is the product of the excited electrons transferring there energy to the material lattice.[14] Exfoliational sputtering is expected to occur when the linear thermal expansion of the material is high, and the laser fluence is not high enough for the target surface to exceed its melting temperature (T_m). Thermal shocks induced by the laser pulses cause deformation on the target surface, which can lead to abnormally shaped particulates being carried toward the target by the plasma plume.[1] Hydrodynamic sputtering is prominent in the PLD of metals and metal alloys. The result of hydrodynamic sputtering is that the thin films will exhibit spherical droplets. The droplets form due to the transient melting of a target with surface roughness.[14] There are many methods to reduce the occurrence of the droplets, such as polishing of the target before ablation, using a highly dense target, and rotating the target so that any surface modifications due to the laser is minimized.[15]

The presented sputtering processes are a result of various variables; the ablation process can be generalized if we consider it to be characterized as just thermal process. This allows us to use equation 3.11 to find the

needed laser fluence for vaporization, and ultimate calculate the mass ablated during the thermal stage. The mass ablated *(m_{abl})* is:

$$m_{abl} = MS_{foc} \int_{t_0}^{\infty} (nv)_{eq} dt \tag{3.12}$$

(M) is the target's atomic mass, *(S_{foc})* the laser spot area and where

$$(nv)_{eq} \propto n_{vap} \left(\frac{2T}{M}\right)^{\frac{1}{2}} \exp\left(-\frac{E_b}{T}\right) \tag{3.13}$$

(T) is the temperature of the ablated particles, and *(n_{vap})* is the density of the saturated vapors close to the solid-vapor interface.[8]

3.3 Plasma Plume Formation

Various experiments and models attempt to understand plasma plume formation in different mediums.[16, 17] These models give insight to plasma plume formation down to the picosecond time scale and with different imaging techniques can provide visual aids. Usual laser flux densities required for most materials to generate a plasma plume are greater than 10^5 W/cm^2.[18] When the ablation threshold is reached, the ejection of electrons, ions, and neutral particles form a shock wave followed directly by the plasma plume; typical temperatures of these plasmas can be in excess of tens of thousands of kelvin.[16, 19] The material plasma vapor plume becomes apparent in the nanosecond time scale and has a supersonic propagation velocity of approximately 10^6 cm/s.[17]

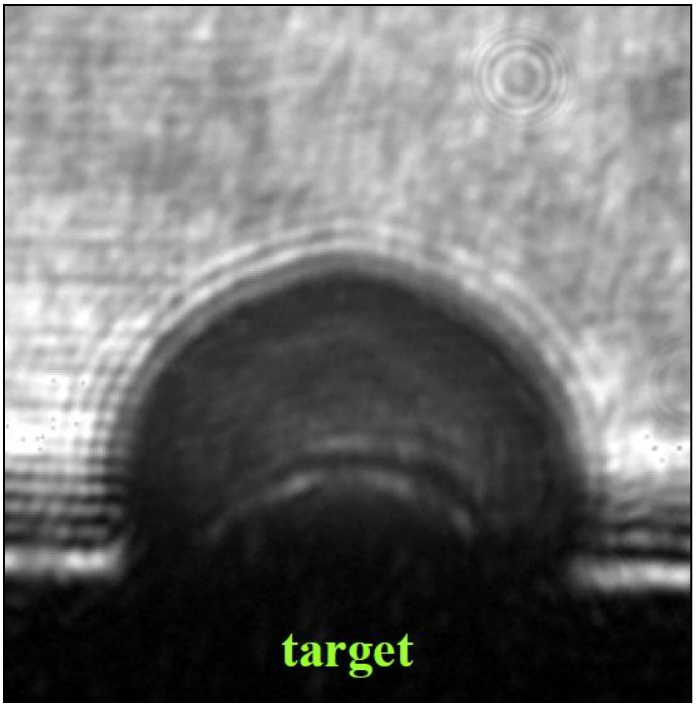

Figure 3.1. Shadowgraph of plume at 1200ps
Source:[17]

The amount of target material present in the plume can be calculated as a vaporization flux (atoms/cm^2 s) using the Hertz-Knudsen equation:

$$u_{vap} = \frac{1}{\rho}\,\beta\,p_0(T_s)\,(\frac{M}{2\pi k T_s})^{\frac{1}{2}} \tag{3.14}$$

where *(T_s)* is the target surface temperature in kelvin, *(β)* the evaporation coefficient, *(ρ)* is the target density, *(M)* target mass in kilograms, *(k)* is Boltzmann's constant, and *($p_0(T_s)$)* is the equilibrium vapor pressure at *(T_s)* in pascals.[20] It is also possible to calculate the ion *(n_i)* to neutral *(n_n)* particle ratio in the plasma plume by using the Eggert-Saha equation:

$$\frac{{n_i}^2}{n_n} = (\frac{2\pi m_e kT}{h^2})^{\frac{3}{2}}\,exp^{(\frac{-E_i}{kT})} \tag{3.15}$$

with *(m_e)* being the electron mass, *(h)* is Planck's constant, and *(E_i)* the ionization energy.[21] In addition to the ion-neutral ratio the electron density has been approximated using experimental techniques and can be expressed as:

$$N_e(z) \approx \frac{2\epsilon_0 m_e \omega^2 \lambda \, q(z)}{e^2 l(z)} \tag{3.16}$$

where *(q(z))* and *(l(z))* respectively correspond to the average phase shift and width of the plasma at a distance *(z)*; *(ε_0)* is the vacuum permittivity, *(e)* electron charge, (*ω)* and *(λ)* are the angular frequency and wavelength of a probe beam.[17]

3.4 Nucleation and Growth of Thin Films

The Volmer-Weber, Frank-van der Merwe, and Stranski-Krastinov nucleation and growth modes explain the nucleation and growth of thin films close to thermodynamic equilibrium. Each growth mode is governed by the balance between the free energies of the film surface *(γ_F)*, substrate surface *(γ_S)*, and the film-substrate interface *(γ_I).*[22] For the Volmer-Weber mode there is no bonding between the film and substrate because the total surface energy is greater than the substrate energy, $\gamma_F + \gamma_I > \gamma_S$; this results to 3-dimensional island growth. When $\gamma_F + \gamma_I < \gamma_S$ this is characterized as Frank-van der Merwe growth mode.[22] Through nucleation and island clustering these films grow as full-monolayers with strong bonding between the film and substrate, they are a monolayer thick and completely combine before

other island clusters develop to form the next monolayer.[23] The Frank-van der Merwe growth mode is characteristic of homoepitaxial thin film growth. The Stranski-Krastinov mode can occur during heteroepitaxial growth due to the lattice mismatch between the substrate and deposited thin film.[22] Initially the growth is monolayer but becomes 3-dimensional island growth due to a biaxial strain induced by the lattice mismatch.[23] Figure 3.2 is a schematic depiction of each growth mode.

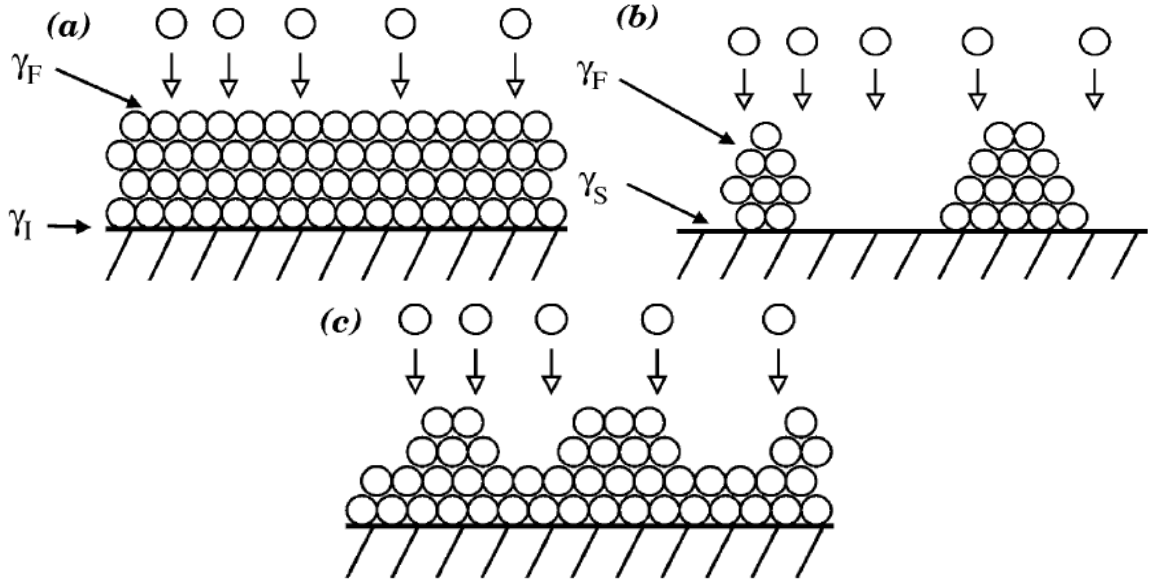

Figure 3.2. *Growth Modes: (a) Frank-Van der Merwe; (b) Volmer-Weber; (c) Stranski-Krastanov*
Source: [22]

The following thin film growth modes provide us with a good understanding of the nucleation, growth, and morphology of thin film growth when close to thermodynamic equilibrium. When films are not grown close to thermodynamic equilibrium, kinetic effects will lead to different growth

modes; addition information pertaining to kinetic type growth modes can be found in [22].

Chapter 4: Pulsed Laser Deposition of Strontium Ruthenate Thin Films

4.1 Introduction

The superconducting state of Strontium Ruthenate (Sr_2RuO_4) single crystals was discovered in 1994 by Yoshiteru Maeno et al. and has a critical temperature of T_c = .93K.[24] The perfection of the crystal growth process has led to a higher superconducting transition of T_c = 1.5K for the best quality single crystals.[25] Also, it has been shown that if lamellar micro-domains of ruthenium metal are embedded into Sr_2RuO_4 or if pure Sr_2RuO_4 is under a uniaxial pressure, the critical temperature is increased T_c = 3-3.5K.[26, 27] The discovery of the superconductivity of Sr_2RuO_4 answered the question if superconductivity can occur in compounds without copper. Since its discovery Sr_2RuO_4 still remains the only non-cuprate superconducting ruthenate. Sr_2RuO_4 is a layer perovskite and a member of the Ruddlesden-Popper homologous series of the general formula $A_{n+1}B_nO_{3n+1}$ with n = 1.[28] Sr_2RuO_4 has a tetragonal structure with a I4/mmm space group and lattice constants at 295K of: a=3.8694(4)Å and c=12.746(2)Å.[29]

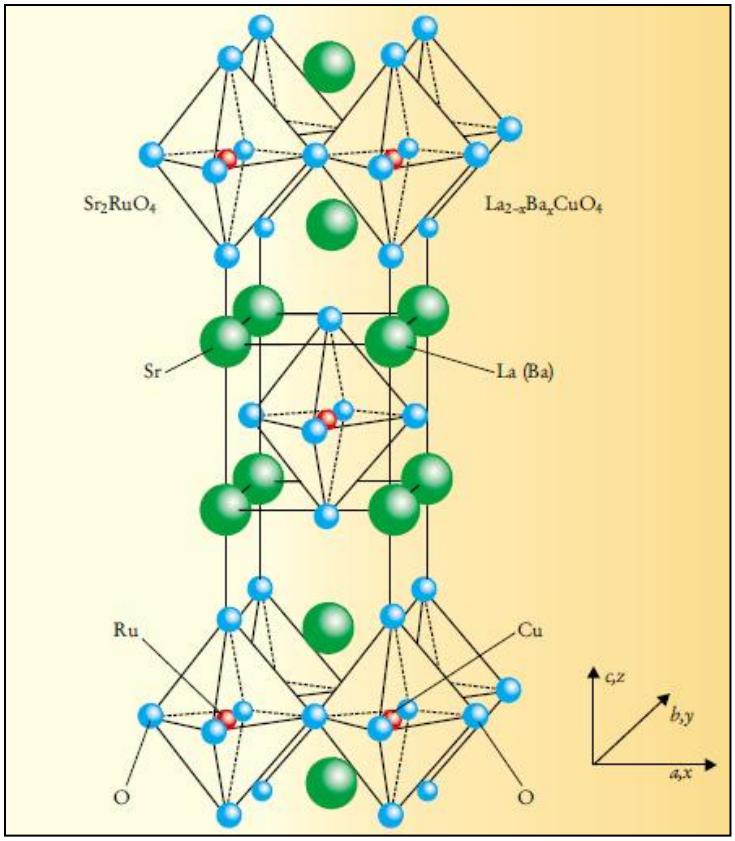

Figure 4.1. Sr_2RuO_4 Layered Perovskite Crystal Structure
Source: [30]

Figure 4.1. illustrates the crystal structure of Sr_2RuO_4. Sr_2RuO_4 has the same perovskite layered structure as the high temperature superconductor (HTS) $La_{2-x}Ba_xCuO_4$.[30]

4.2 Applications for Sr_2RuO_4

Initially, before discovering that Sr_2RuO_4 was superconductive it was used as a substrate for the epitaxial thin film growth of the HTS $YBa_2Cu_3O_{7-\delta}$.[31] $SrTiO_3$ at the time was the most utilized substrate for HTS thin films, but was limited because it is an insulator and needed to be doped with Niobium (Nb) to make it electrically conductive for device applications of HTS.[30] A need for a highly conductive substrate that would be

compatible with HTS led to the idea that Sr_2RuO_4 could be used, because at the time no other substrate met these criteria. The two main reasons for considering Sr_2RuO_4, was that it was highly conductive along the ab-plane and a very stable compound; secondly the lattice constants were a 1.3% better match than $SrTiO_3$.[30, 31] Sr_2RuO_4 as a substrate has a potential device application in field effect transistors (FET), where it would serve as a gate electrode.[30]

Epitaxial Sr_2RuO_4 thin films produced, until recently had not exhibited superconductive properties.[28, 32] The superconductivity of these films were suppressed by impurities in the target material and crystallographic defects in the thins films.[32] Currently, the only superconductive Sr_2RuO_4 thin films ever produced, were produced in 2010 by Y. Krockenberger et al., their Sr_2RuO_4 thin films have a T_c = .6K. The success of growing superconducting Sr_2RuO_4 thins films will allow experiments to verify p-wave symmetry of the superconductivity order parameter and introduce new applications for superconducting electronics, specifically the use as a normal metal in superconductor-normal metal-superconductor (SNS) Josephson junctions.[28, 33]

4.3 Experimental Procedure

The primary purpose for the PLD of Sr_2RuO_4 thin films for this thesis is to explore the possibility of growing superconductive thin films under a specific set of growth parameters. The neodymium-doped yttrium aluminum

garnet (Nd^{3+}: YAG or Nd:YAG) LOTIS TII LS-2147 pulse laser system was used for the deposition of the Sr_2RuO_4 thin films. The Nd:YAG laser system operated at 266nm, with a pulse width between 14-15ns, at a repetition rate of 2 hertz (Hz). Prior to the deposition of the Sr_2RuO_4 thin films a cut silicon wafer was irradiated by the laser beam to determine the area of the laser spot. Due to working parameters of the deposition chamber, laser system, and focusing lens (Newport biconvex lens) the resulting laser spot was a line. By using a microscope to magnify the spot and taking measurements with a measuring caliber, with aid of the imaging software ImageJ the area of the spot was determined to be 1.875mm^2. This data was then used to determine the diameter of a circular spot with equal area; the diameter was calculated to be 1.54mm this information was then inputted in a laser meter to determine the laser fluence.

A Sr_2RuO_4 disk with a 25mm diameter and 6mm thickness was the target material. Fill in the details for the production process. The substrates chosen for the deposition of Sr_2RuO_4 were lanthanum aluminate ($LaAlO_3$ or LAO) and strontium titanate ($SrTiO_3$ or STO); both of the substrates were purchased from MTI Corporation. The LAO substrate was grown by the Czochralski method and has a <100> orientation with lattice constant a=3.821Å above 435°C; the area of the LAO substrate is 100mm^2. The Vernuil method was used to grow the SRO substrates, they also have <100> orientation and a lattice constant of a=3.905Å; the STO substrate has an

area of 50mm^2. Both of the LAO and STO substrates were chosen based on their lattice parameters which closely match the Sr_2RuO_4 of *a*=3.8603(5)Å.

Two Sr_2RuO_4 thin films were produced and both had different growth conditions; on-axis geometry was used for the deposition of the films. For the first deposition, the STO substrate was chosen and the thin film was labeled as S_2RO_4/STO. Using the vacuum pump configuration discussed in chapter 2 section 4.2 the initial pressure of the deposition chamber was pumped down to 8.3 X 10^{-8} Torr. The substrate was then heated to 818.9°C and 1 millitorr (mT) of ultra high purity oxygen gas (O_2) was introduced into the deposition chamber, the pressure in the chamber after this stabilized at 10^{-3} Torr. The target-to–substrate distance was set to 50mm, during deposition the target and substrate rotated in a clockwise direction at equal velocities. The rotation of the substrate ensures that the thin film deposits with uniformity, the rotation of the target material decreases target erosion and consumption due to the laser. It has also be shown that the rotation of the target decreases the deposition of particulates on the substrate and leads to thin films with a decrease in roughness.[1] The S_2RO_4/STO film was produced under a fluence of .63 J/cm^2±2%, this translates to a power density between 4.2 X 10^7 and 4.5 X 10^7 W/cm^2. The deposition time for the S_2RO_4/STO thin film was 2 hours, the substrate temperature during deposition varied from 818.9 - 830.1ºC.

The second thin film was deposited on the LAO substrate; as before the target-to-substrate distance was set to 50mm and rotation of the target and substrate were the same. The initial pressure before heating the substrate was 6.3 X 10^{-8} Torr. Heating of the LAO substrate was set to 777.6°C and again 1mT of ultra high purity O_2 gas was introduced into the deposition chamber. Before deposition the pressure in the chamber was allowed to stabilize at 10^{-3} Torr, the fluence used to deposit the S_2RO_4/LAO thin film was .83 J/cm^2±2%. The power density was between 5.5 X 10^7 and 5.9 X 10^7 W/cm^2, the deposition time remained 2 hours and the substrate temperature during deposition was 777.6 - 815.2°C. For both thin films after deposition they were allowed to reach room temperature under vacuum.

Energy-dispersive X-ray spectroscopy (EDS or EDX) measurements were conducted on a JEOL 5410 conventional scanning electron microscope (SEM) equipped with an EDAX EDS spectrometer to verify the composition of the Sr_2RuO_4 target. Field emission scanning electron microscopy (FESEM) images were taken on a Zeiss LEO 1530VP FESEM to examine the target and thin film surfaces. The PANalytical X'Pert Pro X-ray diffraction (XRD) system was used to do θ-2θ scans on the S_2RuO_4 target to examine target quality, on the substrates to confirm orientation and the produced thin films for characterization. Resistance measurements of both the S_2RO_4/STO and S_2RO_4/LAO thin films were made using a Quantum Design Physical Property Measurement System (PPMS) utilizing a four-wire resistance method; the

samples were mounted on a resistivity puck using GE varnish, contacts were made with four 28 gauge copper wires and PELCO high performance silver paste.

4.4 Results and Discussion

The FESEM image of the Sr_2RuO_4 target shows that the surface is granular with particle size on average of 3μm.

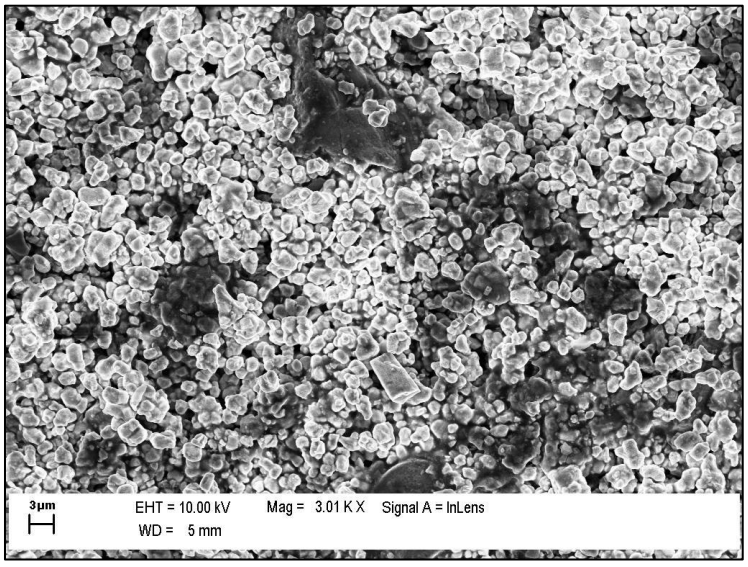

Figure 4.2. FESEM of Sr_2RuO_4 Target Surface

The EDS measurement of the Sr_2RuO_4 target shows that based on the molecular weight percentages the target exhibits correct composition.

Table 4.1. EDS measurement of Sr_2RuO_4 Target

Element	*Wt%*
OK	16.32
SrL	55.79
RuL	27.89

The XRD scan of the target also confirms that the target is of correct composition. A labeled XRD scan of the Sr_2RuO_4 polycrystalline orientations can be found in the appendix a.

Figure 4.3. θ-2θ XRD scan of Sr_2RuO_4 Target

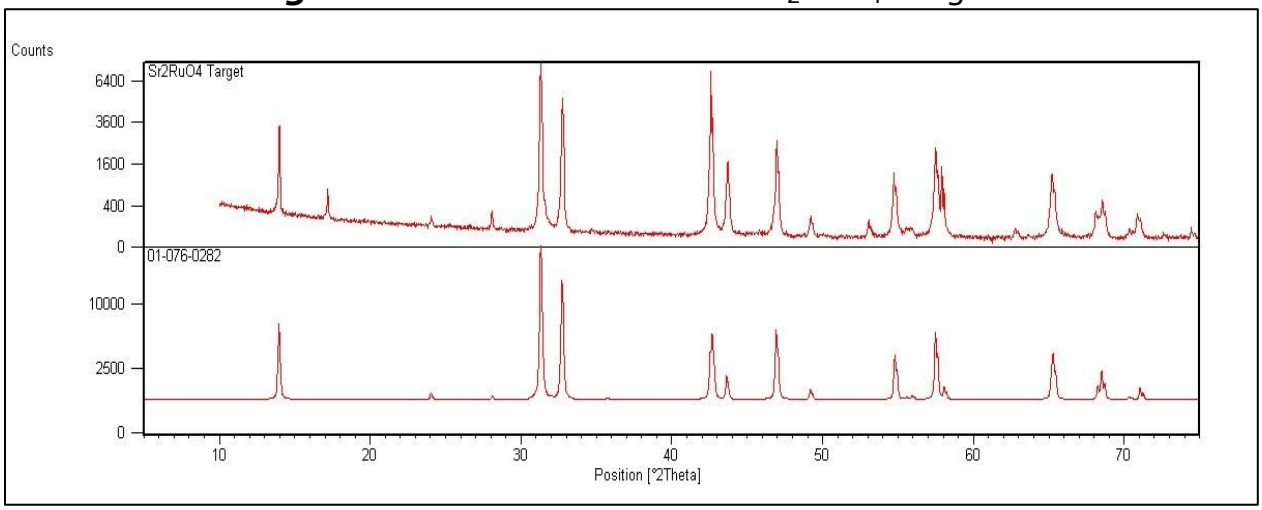

Figure 4.4. θ-2θ XRD scan of STO and LAO substrates

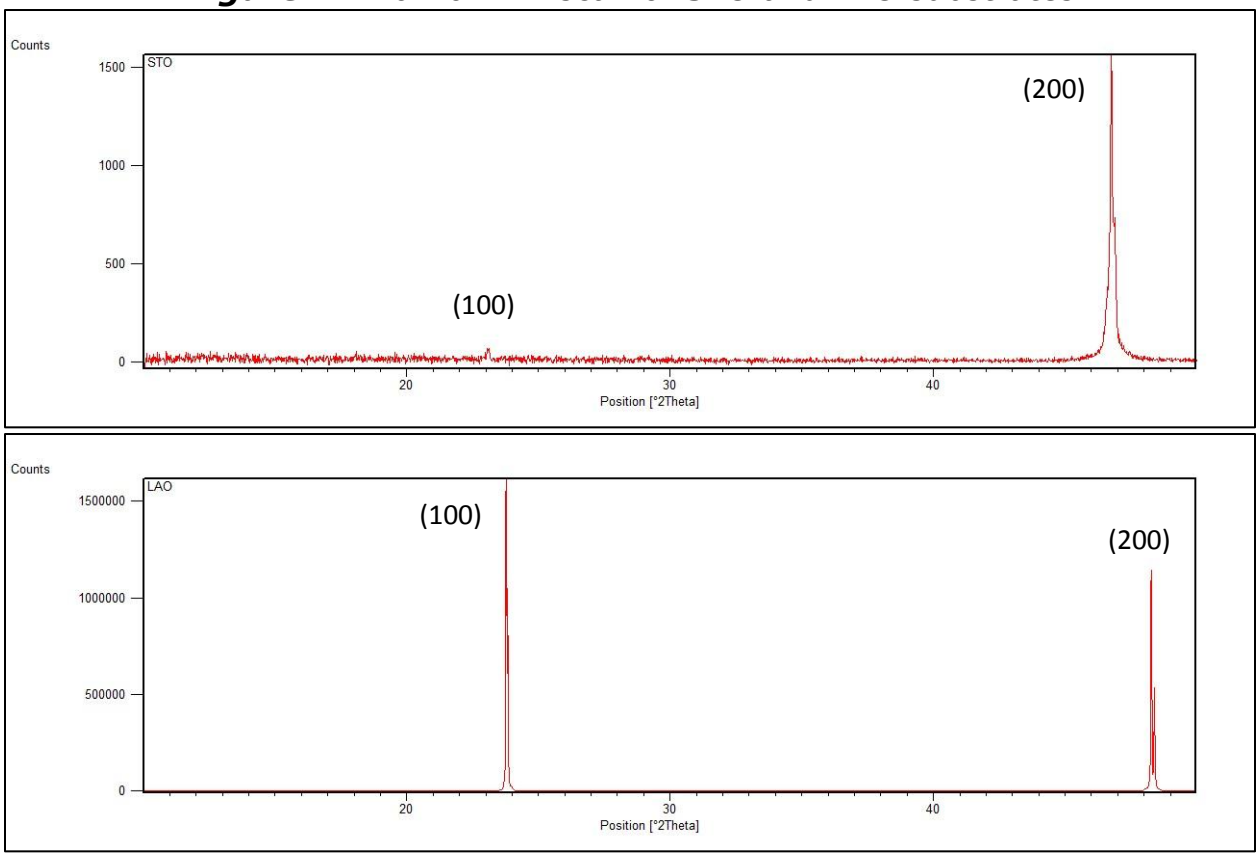

XRD scans are particularly important for determining if the thin films produced show epitaxial crystalline structure growth. If the films do not exhibit this epitaxial growth than the produced S_2RuO_4 thin films will not show superconductive properties. It is important to state that when the thin films were removed from the deposition chamber they had a powder layer above a stable thin film layer that was removed with a KimWipe before all measurements were done. The mechanism responsible for this powder layer is unknown. The XRD scans of both the S_2RO_4/STO and S_2RO_4/LAO thin films show that the films are not of epitaxial growth. The S_2RO_4/STO XRD scan shows that the film is amorphous, due to the lack of any c-axis oriented peaks, which would have indicated a film of epitaxial growth.

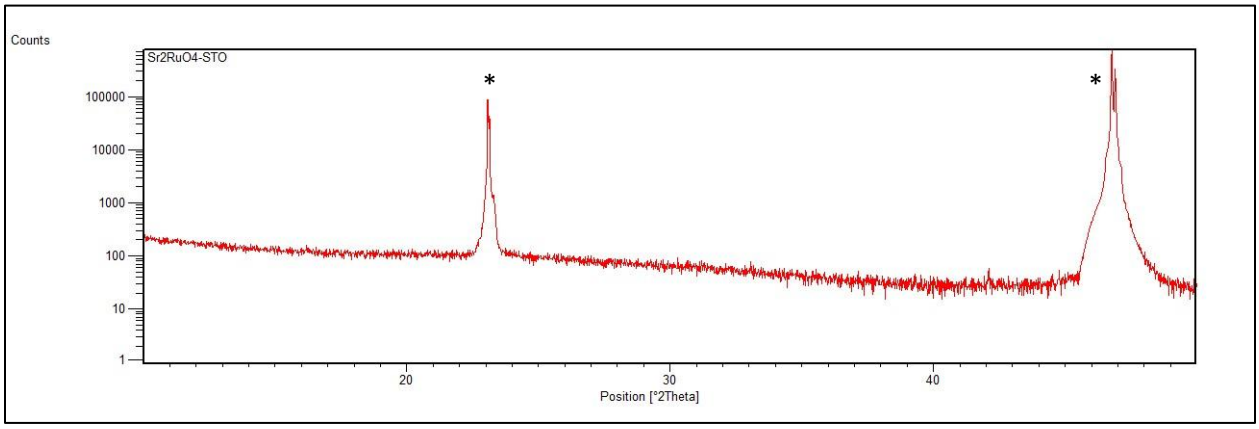

Figure 4.5. θ-2θ XRD scan of S_2RO_4/STO thin film. The STO peaks are marked (*)

The S_2RO_4/LAO scan shows that there was polycrystalline growth, but not the favored epitaxial growth for films that could show superconductivity.

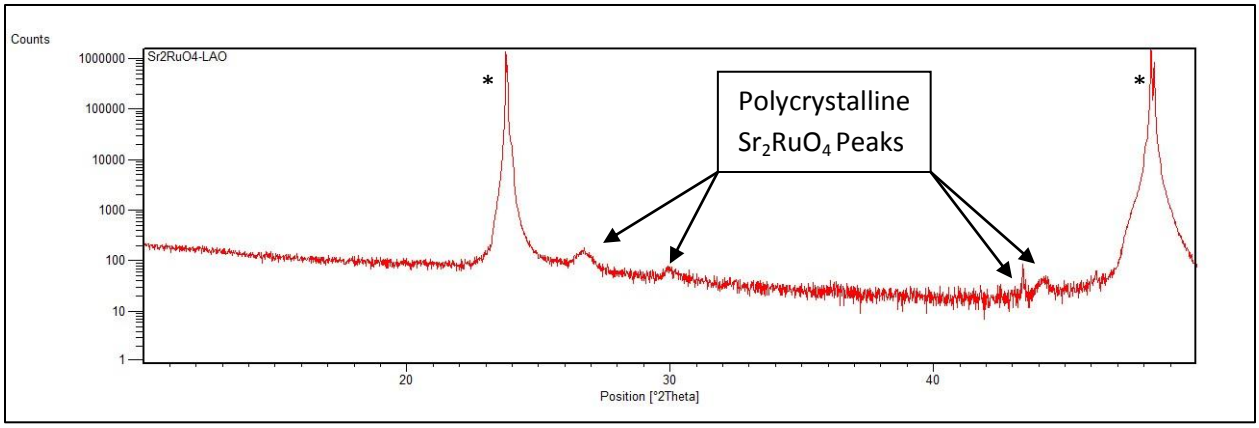

Figure 4.6. θ-2θ XRD scan of S_2RO_4/LAO thin film. The LAO peaks are marked (*)

The resistance measurements of both the S_2RO_4/STO and S_2RO_4/LAO films were measured as a function of temperature, from room temperature to 65K for S_2RO_4/STO and to 35K for S_2RO_4/LAO. The resistance measurements show that both films have semiconducting behavior. The reason for the semiconducting behavior is unknown but is most likely due to the growth conditions. This type of behavior has been exhibited before in epitaxial S_2RuO_4 thin films but the mechanism for this semiconducting characteristic was also unclear.[28] Observing the FESEM images it is apparent that the produced thin films were not continuous and this could have also contributed to the semiconducting behavior.

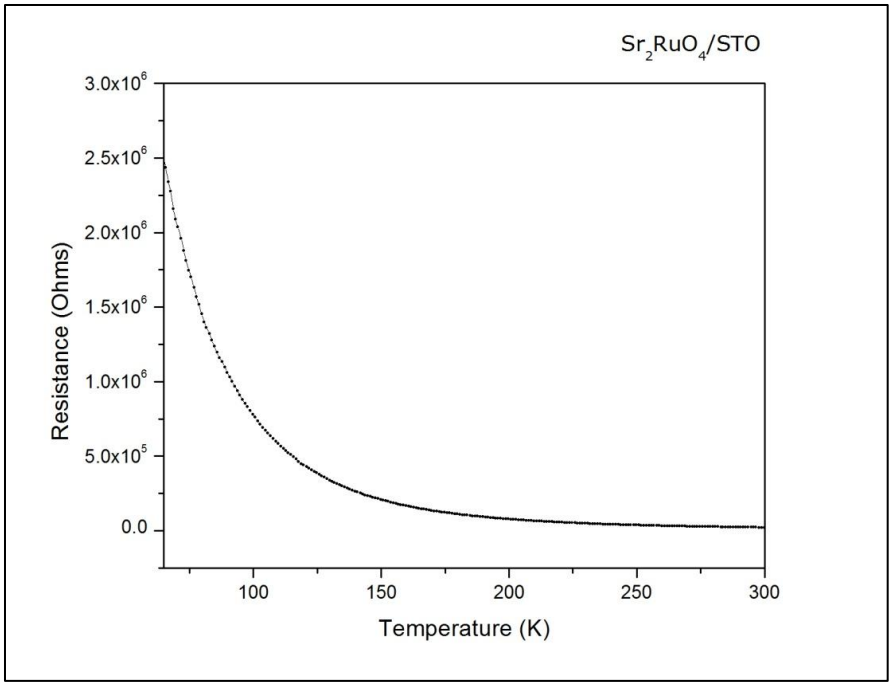

Figure 4.7. Resistance Measurement for Sr_2RuO_4/STO

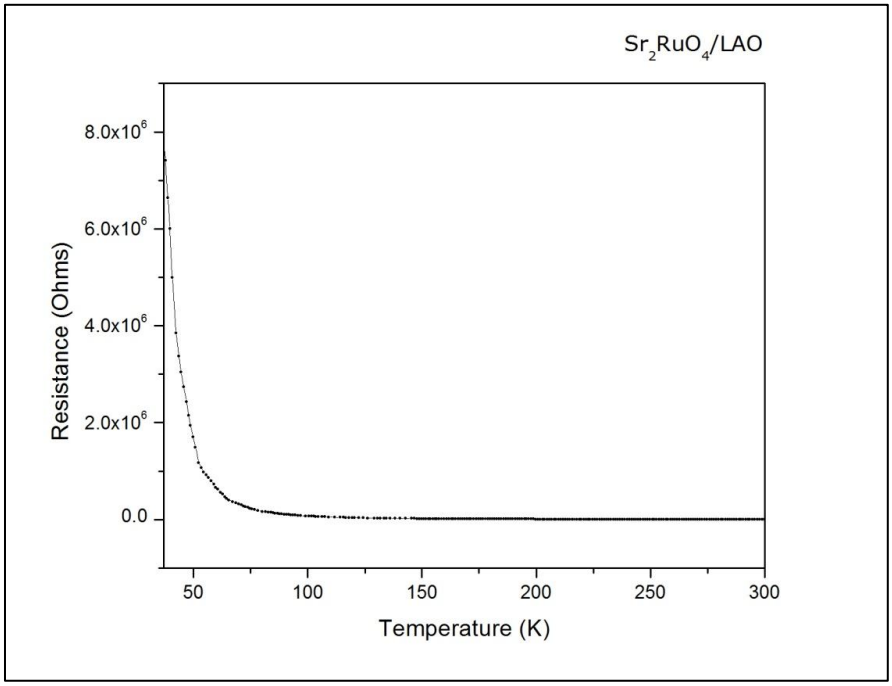

Figure 4.8. Resistance Measurement for Sr_2RuO_4/LAO

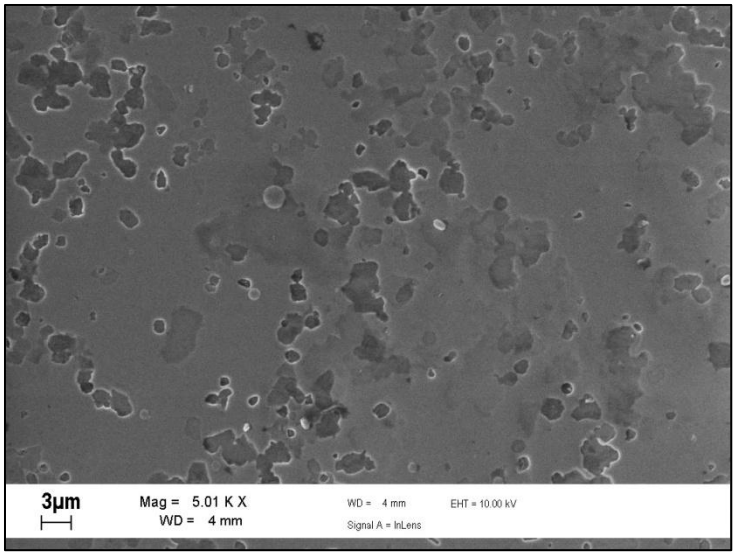

Figure 4.9. FESEM of S_2RO_4/STO Surface

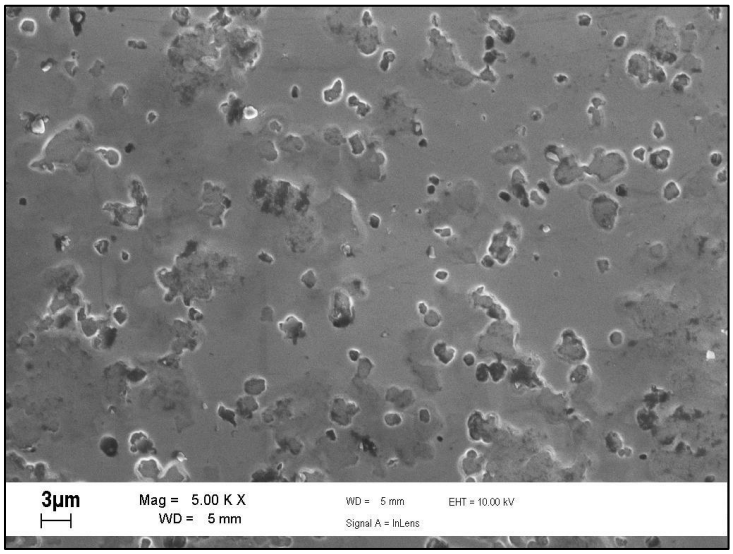

Figure 4.10. FESEM of S_2RO_4/LAO Surface

4.5 Conclusion

Sr_2RuO_4 amorphous and polycrystalline thin films have been produced using PLD under a specific set of conditions as indicated by XRD scans. Although the resulting growth conditions did not produce epitaxial superconducting Sr_2RuO_4 thin films it has lead to a greater understanding of the PLD process. The use of only O_2 as a background gas, low energy

densities (fluence), and temperatures between 777.6 - 830.1°C are likely the contributing factors that lead to the existence of the powder layer and non-epitaxial superconductive thin films. Until recently (August 2010), the growth conditions for Sr_2RuO_4 thin films had not been established but it has been found that the addition of argon (Ar) as a background gas, 3 J/cm^2 as the fluence, and deposition temperatures around 920°C are needed for superconducting Sr_2RuO_4 thin films.[33] For future reference, these growth conditions should be considered for the success of growing epitaxial superconductive Sr_2RuO_4 thin films by PLD.

Chapter 5: Pulsed Laser Deposition of Terfenol-D Thin Films

5.1 Introduction

It is known that all magnetic materials to some degree are magnetostrictive but only a small amount of materials have a giant magnetostrictive response.[34] This giant magnetostrictive response exists in materials that contain rare earth elements. The magnetostriction in these materials is a product of the strong magnetoelastic coupling within the material.[34] Magnetostriction can be defined as the deformation of a body in response to change in its magnetization.[34]

Terfenol-D is a giant magnetostrictive material, it was developed by the Naval Ordnance Laboratory in the 1970s and the manufacturing of it was perfected at Ames Laboratory in the 1980s. Terfenol-D was named based on its composition and place of development, terbium (ter), iron (Fe), Naval Ordnance Laboratory (nol), and dysprosium (D).[35] The magnetostriction of Terfenol-D is positive, meaning when placed in an external magnetic field the magnetostrictive expansion will be in the direction of that field. Along with piezoelectrics and temperature sensitive materials, Terfenol-D with its giant magnetostrictive properties is considered a smart material. For a material to be classified as "smart" it must have the ability to sense and react to changes in the surrounding environment.

The purpose of this research is to investigate the magnetoelectric (ME) effect between a magnetostrictive Terfenol-D thin film and an adjoining coupled piezoelectric Lead Titanate ($PbTiO_3$) thin film. What makes Terfenol-D an attractive material to use for this investigation is that at room temperature it has the highest magnetostriction of any material.[36] The Terfenol-D used for this research has a composition of $Tb_{.3}Dy_{.7}Fe_{1.92}$ and is cubic in structure. The lattice constant at room temperature is: *a = 7.35Å,* this lattice constant is based on the XRD data from figure 5.2..

5.2 Applications for Terfenol-D

With Terfenol-D providing a positive, proportional, and microsecond response when placed in a magnetic field, the applications for this type of material are extensive. The driving force for research in highly magnetostrictive materials was their ability to generate a controlled force and motion for underwater sound sources.[37] The magnetostrictive properties of Terfenol-D were first utilized by the United States Navy where it was used to develop higher power sonar with greater bandwidth and reliability.[35] Upon becoming commercially available in the mid 1980s potential applications for Terfenol-D were:

- Sound and vibration sources
- Mechanical impact actuators
- Magnetostrictive motors
- Electric generators

The listed applications above are just a few of the wide range of uses that many have found for Terfenol-D. An elaborate discussion on the applications, and designs for Terfenol-D devices can be found in [37].

For the previous applications many incorporate large amounts of Terfenol-D to make transducers or actuators, with our thin films the applications are for devices in the micro scale. Devices that show promise for applications are micro sensors, actuators, and acoustic-wave devices.[38] In the case of micro-sensors, a Terfenol-D thin film is deposited onto a micro-cantilever to produce a magnetometer with high sensitivity.[39] Terfenol-D thins films as micro-actuators can be valves, or a positioning device.[40]

Another creative device dubbed a micro-traveler can move in a directed path wirelessly in response to a external magnetic field.[41] With the fabrication of magnetostrictive devices being rather simple an interest for their applications has increased. The thin films prepared for this thesis builds on the previous work done by others and establishes a method for producing hybrid multiferroic nanocomposites by PLD for the investigation of magnetoelectric (ME) coupling.

5.3 Experimental Details

An extensive amount of samples and measurements were prepared to investigate the magnetoelectric (ME) effect between the magnetostrictive Terfenol-D (TD) thin film and the adjoining coupled piezoelectric Lead Titanate ($PbTiO_3$ or PTO) thin film. As before a Nd:YAG laser system

operating at 266nm, with a pulse widths between 14-15ns, at a repetition rate of 10 hertz (Hz) was used for PLD; these parameter were used for all the TD thin films produced, the only adjusted parameter was the fluence. As mentioned before in chapter 4 section 3, as a result of working parameters and the focusing lens the projected laser spot on the target was a line. To change this to a more desired circular laser spot a new focusing lens was used to produce the TD thin films, note that the only TD thin film produced using the old focusing lens configuration was TD250/PTO275 as a result the deposition rate was lower than the other films of comparable thickness. The previous lens was replaced by a fused silica plano-convex lens made by CVI Melles Griot and the procedure to determine the laser fluence was the same as described in chapter 4 section 3.

The TD target for the PLD of all thin films was purchased from Etrema Products Inc. and was a disk with a 25mm diameter and 6mm thickness. Before deposition the target was briefly sanded down with 500 grit sand paper, cleaned with ethanol and rinsed with isopropyl alcohol. The reason for sanding down the target was to simulate the target surface characteristics if the target had been used for PLD then again resurfaced for use. The target was then imaged by FESEM to observe the surface to ensure that the target was free of large particulates that could result in TD thin films with a large surface roughness.

The produced thin films were deposited on two types of substrates: a $LaNiO_3$ (LNO) buffered conductive <100> Si substrate with a deposited 275nm PTO layer and the other with a 280nm PTO layer. The PTO layer was deposited on the LNO buffered conductive Si substrate by liquid phase deposition (LPD), the parameters for the LPD process can be found in [42]. The PTO substrates were cleaned prior to PLD with isopropyl alcohol.

The first thin film produced was tagged TD250/PTO275 (samples are tagged according to their thin film thicknesses ex: TD250/PTO275 is a TD film of 250 nm on a PTO thin film of 275 nm), an amorphous TD layer was deposited for 3 hours at a temperature of 24 - 29°C. The target-to-substrate distance was set to 60mm; this distance was used for all of the TD films. The background pressure during PLD of this film was 3.90 X 10^{-7}±.91; the fluence was set to 1.006 J/cm²±2%. The following three thin films: TD39/PTO280, TD203/PTO280, and TD327/PTO280 also have an amorphous TD layer and were deposited at a deposition rate of 2.67 nm/min with the fluence set at 1.032 J/cm²±2%. The temperatures during deposition were 21 - 24ºC, with background pressures at 7.63 X 10^{-7} to 2.18 X 10^{-6} Torr. These three thin films were annealed after deposition at temperatures of 386 - 398ºC in background pressures of 4.8 X 10^{-7} to 1.32 X 10^{-6} Torr.

The thickness of the PTO films was measured by spectral reflectance with the F20 film thickness measurement system from Filmetrics. A Zeiss LEO 1530VP field emission scanning electron microscope (FESEM) was used

to examine the target. Energy-dispersive X-ray spectroscopy (EDS or EDX) measurements were conducted on a JEOL 5410 conventional scanning electron microscope (SEM) equipped with an EDAX EDS spectrometer. The PANalytical X'Pert Pro X-ray diffraction (XRD) system was used to do θ-2θ scans on the target, PTO substrate, and the produced thin films for characterization of phases. The magnetic properties of the produced thin film heterostructures were measured with a Princeton Measurements Corporation Micromag alternating gradient/vibrating sample magnetometer (AGM/VSM). AFM images of the TD/PTO films were done with an Asylum Research MFP-3D atomic force microscope. The AFM was also used to determine the thickness of the TD on the PTO substrates by dragging the AFM tip over the TD and PTO interface. Piezoelectric properties of the thin films were measured by using a silicon tip coated with a 20nm Pt/Ir layer and applying an in-plane magnetic field with a variable field module (VFM), piezoelectric signals were measured with the PFM module of the MRP-3D AFM by using a AC240TM cantilever.

5.4 Results and Discussion

An EDS of the target also confirms the composition based on the molecular weight percentages to be close to $Tb_{.3}Dy_{.7}Fe_{1.92}$. The FESEM image obtained shows that the target surface is relatively flat with small areas of particulates with the larger particles in the size range of 2μm. The XRD θ-2θ

scan of the TD target shows that the target is polycrystalline with multiple phases.

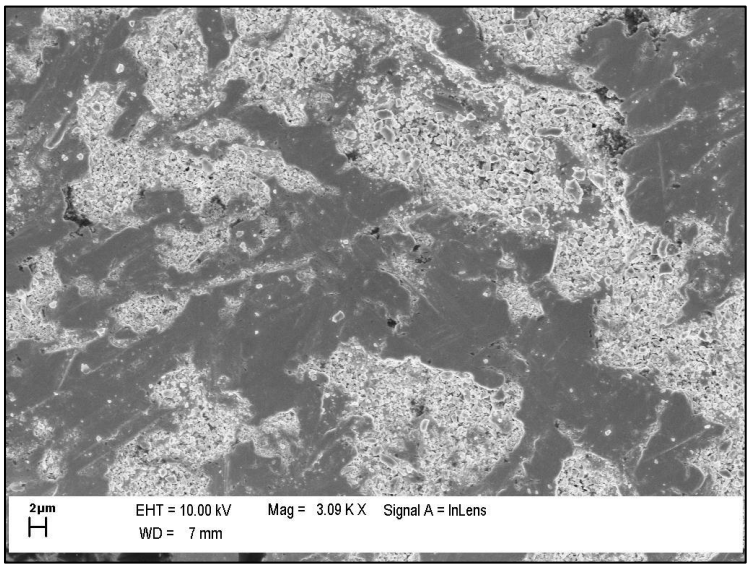

Figure 5.1. FESEM of TD Target Surface

Table 5.1. EDS measurement of Terfenol-D Target

Element	*Wt%*
TbL	15.92
FeK	38.72
DyL	45.36

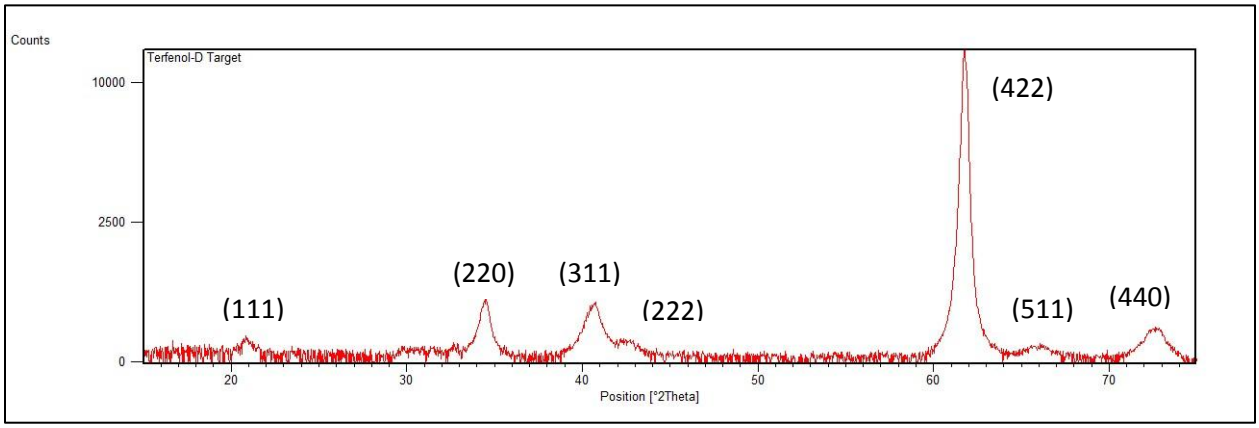

Figure 5.2. θ-2θ XRD scan of TD Target.

The XRD analysis of the PTO thin films has shown that the films are free of impurities and polycrystalline. In figure 5.3. the XRD pattern of the 280 nm PTO is shown. The peaks of the PTO layer are distinguishable despite some overlap with the peaks of the LNO buffer layer.

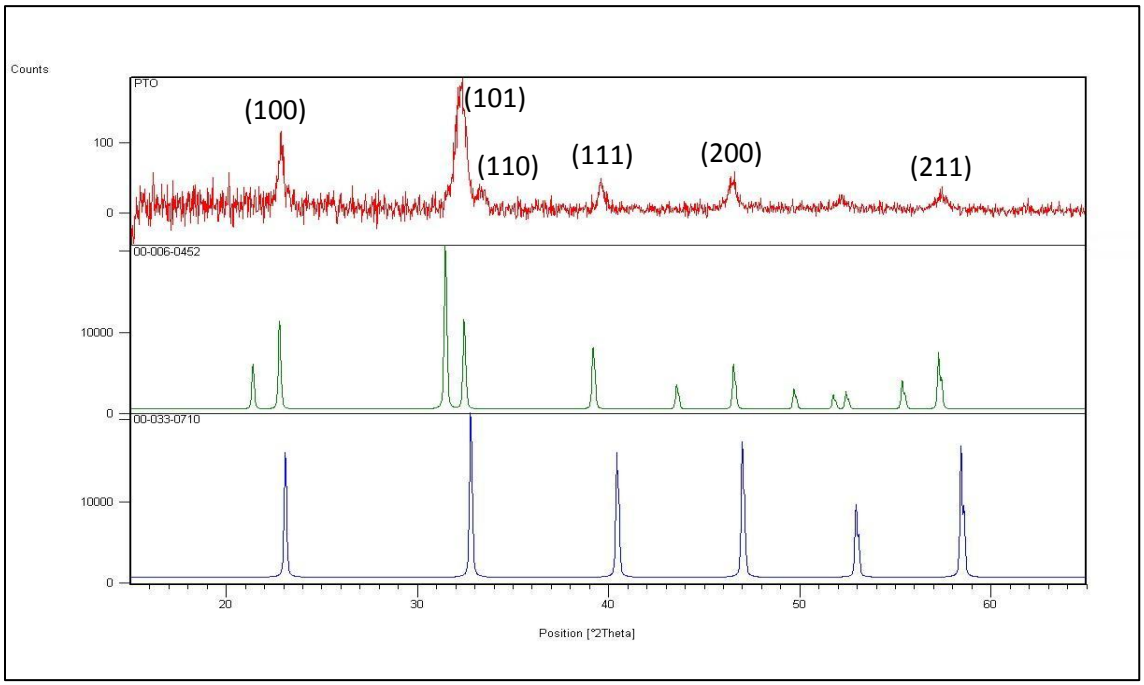

Figure 5.3. θ-2θ XRD scan of 280nm PTO. The green and blue curves represent standard PTO and LNO scans respectively.

AFM images of the 275 nm PTO shows that the thin film is continuous with densely packed grains with an average diameter of 77 nm and a root mean square (rms) roughness of 9.7 nm. The Pb/Ti ratio obtained from inductive plasma coupled spectrometry was .978:1, suggesting that the PTO films are nearly stoichiometric. In figure 5.4a and 5.4b a cross-section FESEM image and AFM topography image can be seen of the 275 nm PTO film.

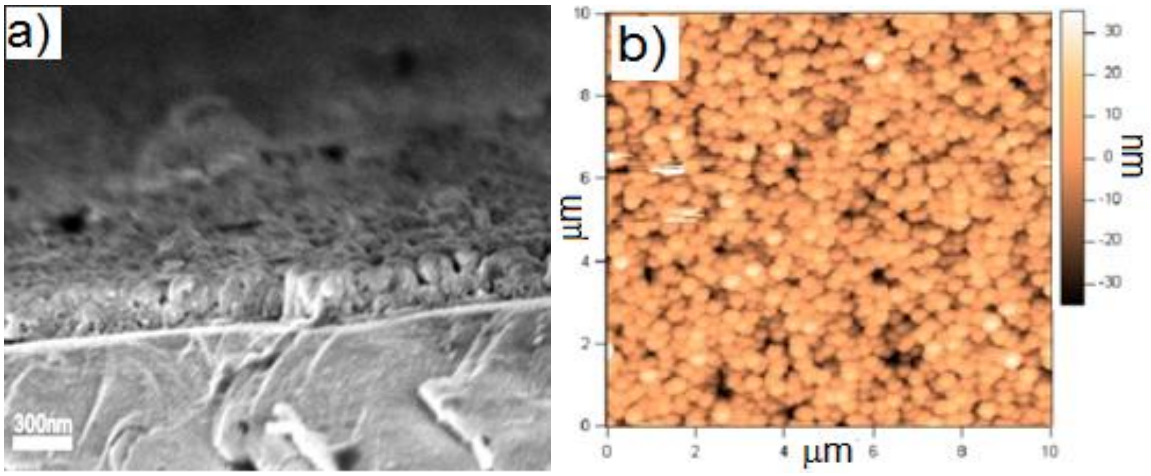

Figure 5.4. Cross-sectional FE-SEM (a) and Topography AFM (b) images of $PbTiO_3$ layer

To investigate the ME coupling between the adjoining PTO and TD layers a novel experimental technique called magnetic field-assisted piezoelectric force microscopy (MFA-PFM) was used.[43] When observing the phase and amplitude components of the piezoelectric signal, if there are changes when a static magnetic field is applied then experimentally this demonstrates the exists of ME coupling between the PTO and TD layers. The following figure is a representation of the thin film heterostructure nanocomposites.

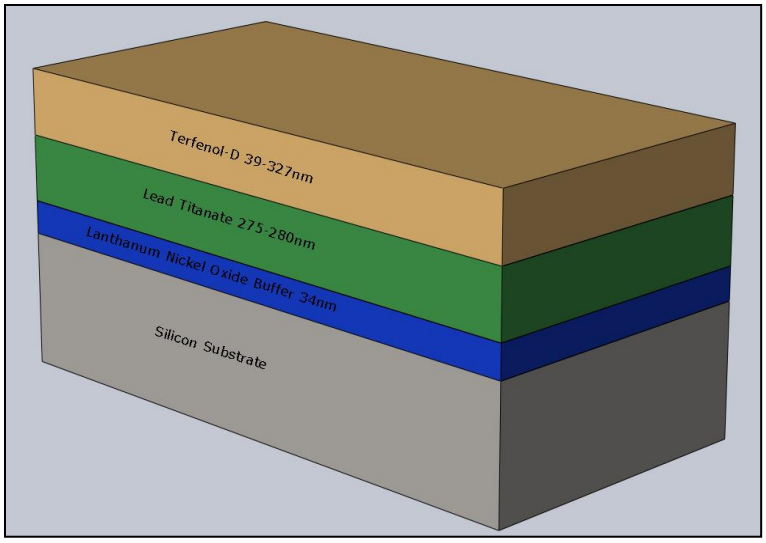

Figure 5.5. Heterostructure Nanocomposite

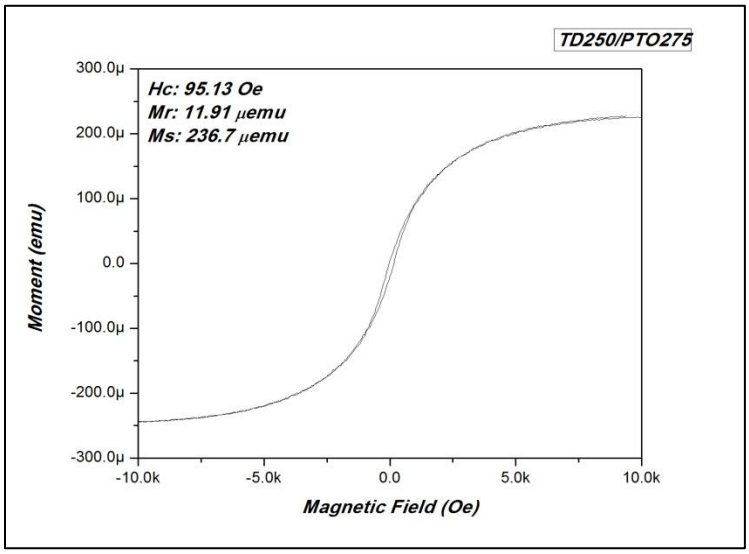

Figure 5.6. VSM Hysteresis of TD250/PTO275

The produced thin films were characterized by XRD, VSM/AGM, AFM, MFA-PFM, and MFM data. In figure 5.6. the applied magnetic field is in plane to the thin film. The XRD data of TD250/PTO275is presented in figure 5.6., the lack of TD peaks is evidence of an amorphous layer. MFM images of the TD250 top layer are shown in figure 5.7 and it is apparent that the TD250 layer is relatively uniform; the rms roughness of the TD250 layer is 18.3 nm.

Also, when the sample is subjected to the represented magnetic fields the topography is unchanged, but the microstructure of the magnetic field changes. The light and dark areas in the MFM images represent the magnetic domains with magnetization up and down respectively. Figure 5.9 and 5.10 display the phase and amplitude plots of the piezoelectric signal of TD250/PTO275 under various magnetic fields.

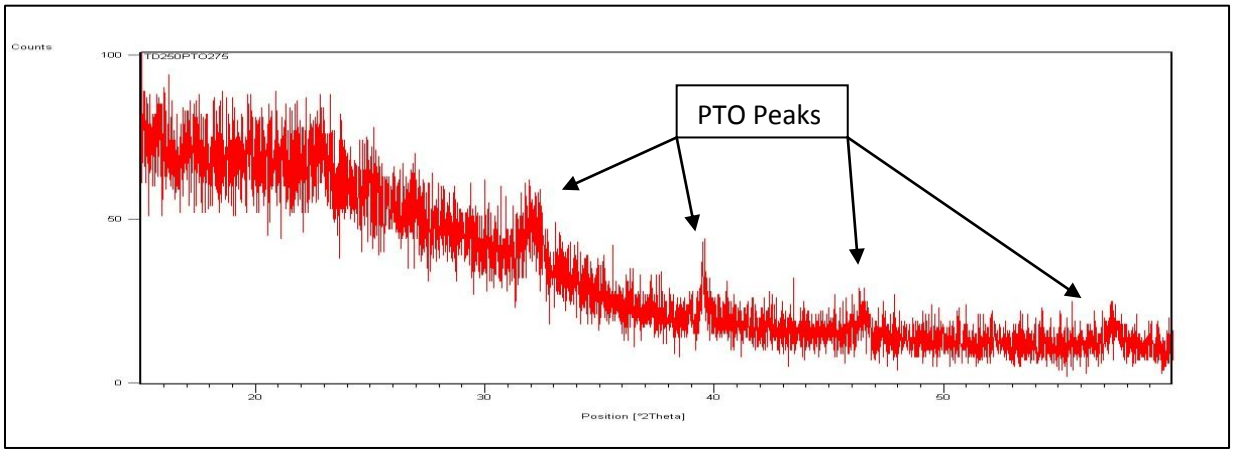

Figure 5.7. θ-2θ XRD scan of TD250/PTO275

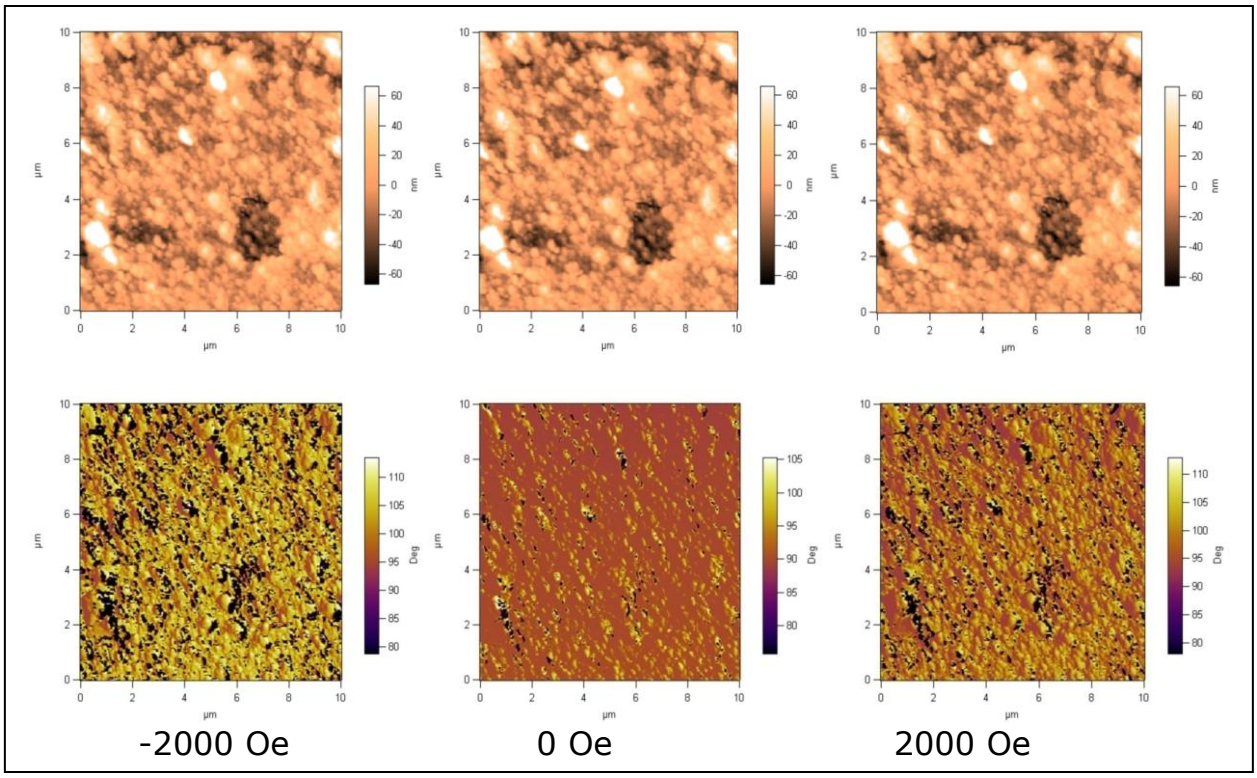

Figure 5.8. AFM and MFM images of TD250/PTO275

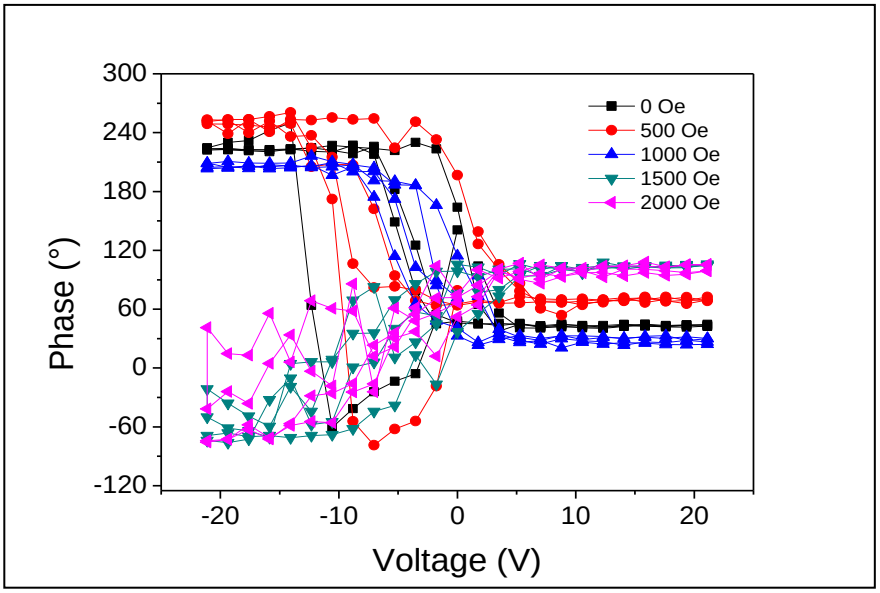

Figure 5.9. Phase Hysteresis Loops of TD250/PTO275

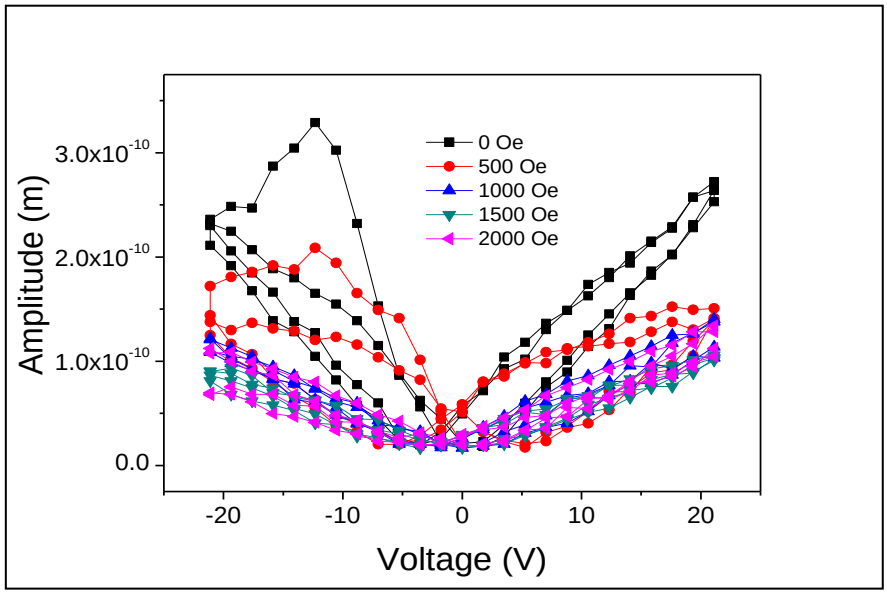

Figure 5.10. Piezoelectric amplitude signal of TD250/PTO275

The phase vs. bias voltage of TD250/PTO275 shows a hysteresis behavior at room temperature, with the difference between the upper and lower phase values close to 180. This indicates the presence of 180 degree domains in the PTO layer. The amplitude vs. bias voltage graph (figure 5.10) exhibits a butterfly-type behavior, this is characteristic of ferroelectric materials. The amplitude in the TD250/PTO275 graph decreases from 267 to 151, 139, 128, and 107 picometers (pm) when the in-plane field increases. Applying a linear fit to a portion of the butterfly loops gives static values for the longitudinal piezoelectric coefficients of d_{33}: 28.3 10.62, 9.3, 8.95, and 8.71 pm/V. The decrease in the d_{33} coefficient of the PTO layer upon the increase of the magnetic field is evidence of ME coupling between the TD and PTO layer. The decrease is attributed to the positive magnetostriction of the TD layer; as the TD layer expands in the direction of the magnetic field it also shrinks perpendicular to the magnetic field. The shrinkage transmits

across the TD/PTO interface and changes the ferroelectric response of the PTO leading to the decrease in the piezoelectric coefficient.

Further investigation of the remaining thin films: TD39/PTO280, TD204/PTO280, and TD327/PTO280 shows that these thin films also have characteristics similar to TD250/PTO275. Again, the XRD data supports that the TD layers are amorphous due to the lack of TD peaks. AFM measurements of the annealed thin films taken at a 0 Oe magnetic field reveal the rms roughness of TD39/PTO280, TD204/PTO280, and TD327/PTO280 are 3.22, 4.27, and 8.79 nm respectively. AGM measurements of the annealed samples can be found in the appendix a.

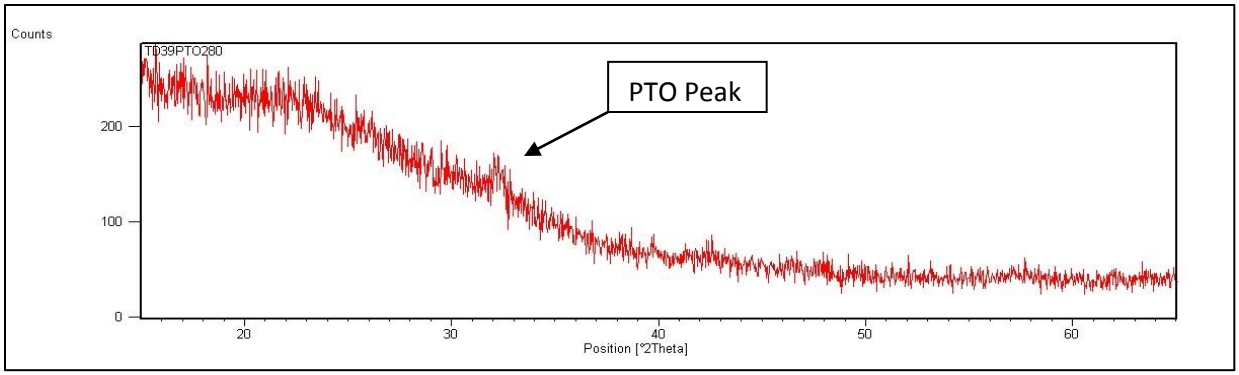

Figure 5.11. θ-2θ XRD scan of TD39/PTO280

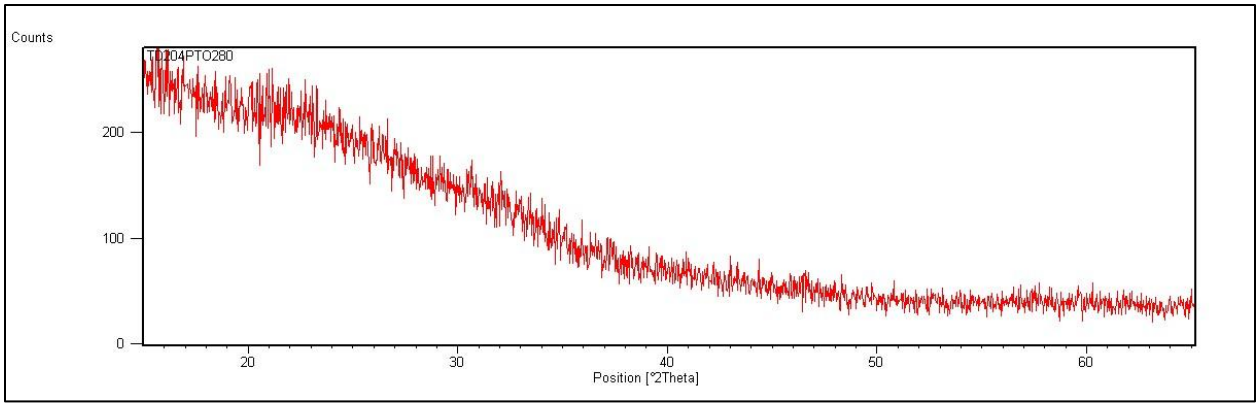

Figure 5.12. θ-2θ XRD scan of TD204/PTO280

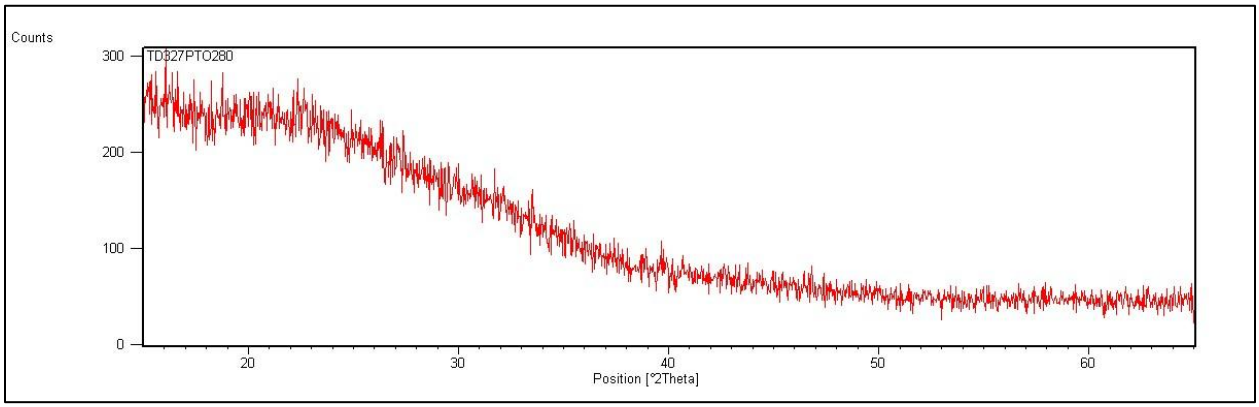

Figure 5.13. θ-2θ XRD scan of TD327/PTO280

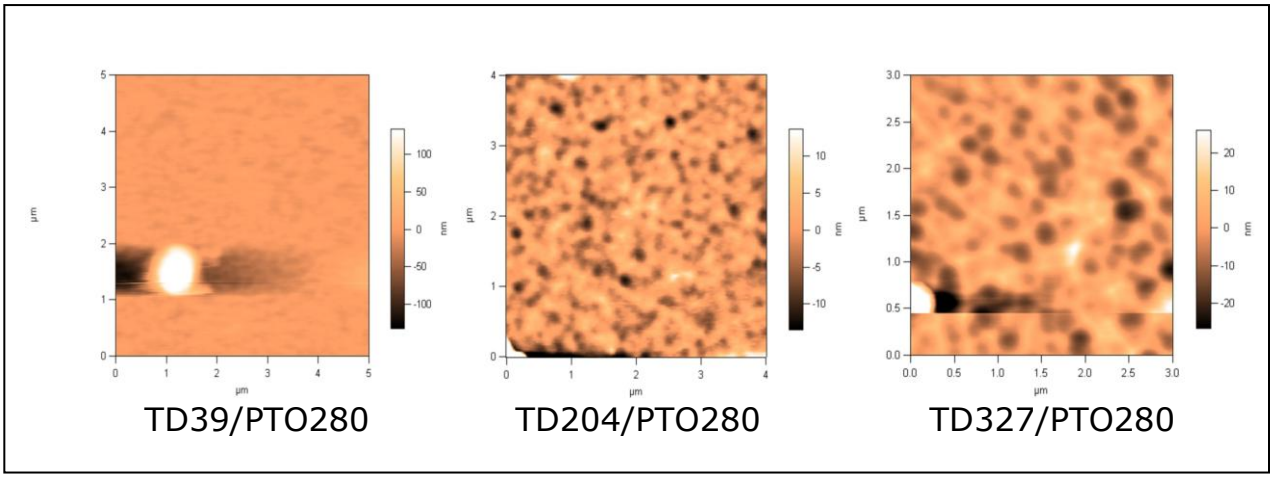

Figure 5.14. AFM images of Annealed Samples

As before the MFA-PFM graphs provide experimental proof of ME coupling between the TD/PTO layers. In the phase vs. bias voltage plots the

change in the hysteresis loop indicates a direction change of polarization of the PTO layer and this is evidence of ME coupling between the layers. In the butterfly loops the amplitude in annealed samples also decreases systematically when the in-plane field increases. In table 5.2 this is represented.

Sample	*Field (Oe)*	*Amplitude (pm)*
TD39/PTO280	0,300,600	572, 482, 423
TD240/PTO280	0,500,1000,1500	528,420,375, 198
TD327/PTO280	0,500,1000,1500	2084, 1370, 937, 755

Table 5.2. Amplitude vs. Bias Voltage Data for Annealed Samples

After apply a linear fit to a portion of the butterfly loops for the annealed samples gives the static values for the longitudinal piezoelectric coefficients which exhibit a decrease, this is represented in table 5.3..

Sample	*Field (Oe)*	*d_{33} (pm/V)*
TD39/PTO280	0,300,600	25.03, 23.52, 22.22
TD204/PTO280	0,500,1000,1500	43.49, 39.09, 25.02, 4.24
TD327/PTO280	0,500,1000,1500	132.81, 95.55, 64.09, 49.91

Table 5.3. Piezoelectric Coefficients for Annealed Samples

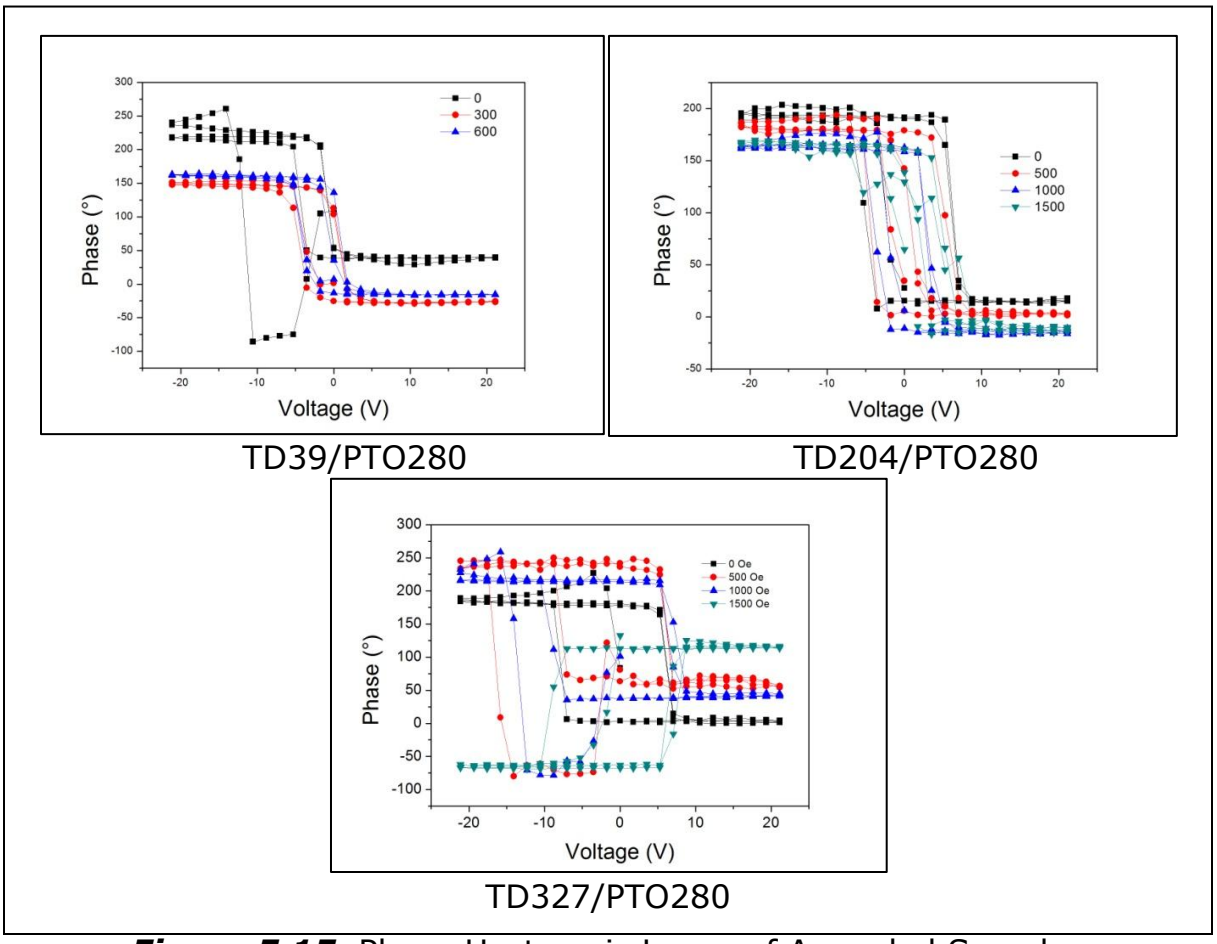

Figure 5.15. Phase Hysteresis Loops of Annealed Samples

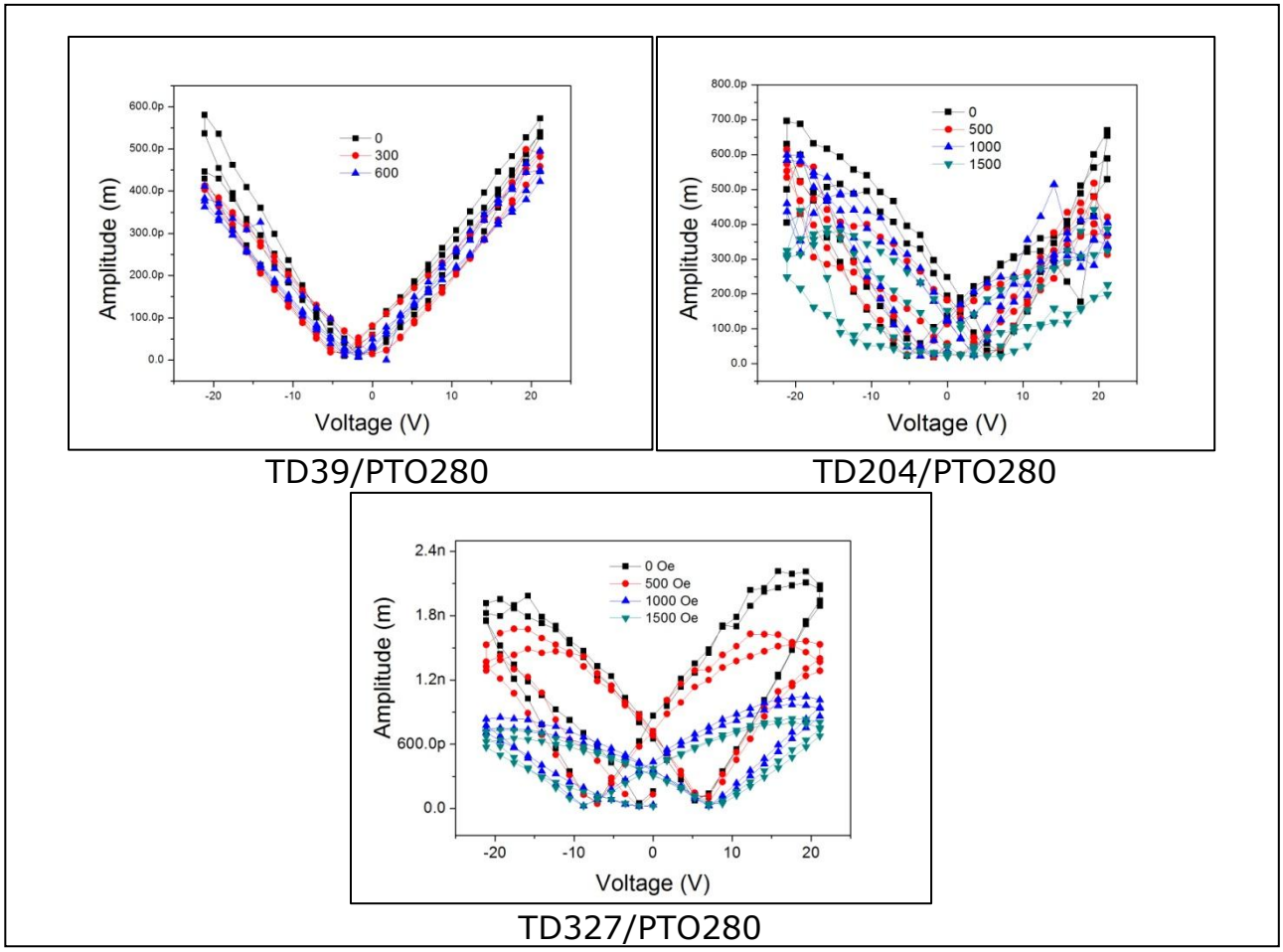

Figure 5.16. Piezoelectric amplitude signal of Annealed Samples

5.5 Conclusion

TD/PTO heterostructure nanocomposite thin films have been produced using PLD. By using the MFA-PFM technique, ME coupling in multiferroic thin films was probed experimentally for the first time. It was found that by increasing the magnetic field in a positive magnetostrictive material this will decrease the d_{33} coefficient in a piezoelectric material.

Chapter 6: General Conclusion

In the 1960's Smith and Turner introduced the PLD method, they showed that this growth method could efficiently produce various types of thin films.[1] With the growth of epitaxial thin films by Cheung in 1983 followed closely by the growth of a high temperature superconductor by Dijkkamp in 1987, these milestones lead to a wide spread interest and practice of producing thin films by PLD.[6, 7] The PLD technique and system are versatile, this allows the user the capability of using different materials to produce many types of thin films; because the system has the ability to establish the necessary environment for the proper deposition those films. With the PLD mechanisms and thin film growth being well understood this adds to the attractiveness for utilizing this technique for the growth of thin films.

Through this research it has been shown that PLD is an effective technique for the production of Sr_2RuO_4 and Terfenol-D/Lead Titanate thin films. Though the produced Sr_2RuO_4 thin films were not superconductive which was the desired result, the growth of the Sr_2RuO_4 thin films led to a greater understanding of the PLD process and necessary knowledge that is needed to characterize thin films. It was concluded that the low purity of the Sr_2RuO_4 target, lattice mismatches between the substrate and Sr_2RuO_4, and growth environment were the contrubiting for the suppression of

superconductivity in the thin films. Modification of the growth conditions based on Y. Krockenberger*, et al.*, "Growth of superconducting Sr2RuO4 thin films" publication the desired superconductive Sr_2RuO_4 thin film result is obtainable.

The investigation of the ME coupling between the Terfenol-D and Lead Titanate nanocomposite thin films was extremely successful. This research was present in Taipei, Taiwan at the 2011 IEEE Intermag conference and resulted in an acceptance for publication in the IEEE Transactions on Magnetics journal. By utilizing a newly developed technique called magnetic field-assisted piezoelectric force microscopy (MFA-PFM) the ME coupling of a multiferroic thin film was measured experimentally for the first time. As a result a better understanding of multiferroic composites was established.

References

[1] J. T. Cheung, "History and Fundamentals of Pulsed Laser Deposition," in *Pulsed Laser Deposition of Thin Films*, G. K. H. Douglas B. Chrisey, Ed., ed New York: John Wiley & Sons, Inc., 1994, pp. 1-22.

[2] A. P. Steven M. Green, K.S. Harshavardhan, J.S. Dernstein, "Equipment," in *Pulsed Laser Deposition of Thin Films*, G. K. H. Douglas B. Chrisey, Ed., ed New York: John Wiley & Sons, Inc., 1994, pp. 24-36.

[3] R. Delmdahl and R. Patzel, "Pulsed laser deposition-UV laser sources and applications," *Applied Physics a-Materials Science & Processing,* vol. 93, pp. 611-615, Nov 2008.

[4] L. TII, "Nd:YAG Laser System LS-2147 User's Manual," ed. Minsk 2006.

[5] C. M. Griot, "All Things Photonic: The CVI Melles Griot Technical Guide," vol. 2, 2009.

[6] J. T. Cheung, "EPITAXIAL-GROWTH OF HG0.7CD0.3 TE BY LASER-ASSISTED DEPOSITION," *Applied Physics Letters,* vol. 43, pp. 255-257, 1983.

[7] D. Dijkkamp*, et al.*, "PREPARATION OF Y-BA-CU OXIDE SUPERCONDUCTOR THIN-FILMS USING PULSED LASER EVAPORATION FROM HIGH-TC BULK MATERIAL," *Applied Physics Letters,* vol. 51, pp. 619-621, Aug 1987.

[8] A. V. R. Eugene G. Gamaly, Barry Luther-Davies, "Ultrafast Laser Ablation and Film Deposition," in *Pulsed Laser Deposition of Thin Films: Applications-Led Growth of Functional Materials*, R. Eason, Ed., ed Hoboken: John Wiley & Sons, Inc., 2007, pp. 99-114.

[9] E. G. Gamaly*, et al.*, "Ultrafast ablation with high-pulse-rate lasers. Part I: Theoretical considerations," *Journal of Applied Physics,* vol. 85, pp. 4213-4221, Apr 1999.

[10] A. V. Rode*, et al.*, "Ultrafast ablation with high-pulse-rate lasers. Part II: Experiments on laser deposition of amorphous carbon films," *Journal of Applied Physics,* vol. 85, pp. 4222-4230, Apr 1999.

[11] S. S. Mao*, et al.*, "Dynamics of femtosecond laser interactions with dielectrics," *Applied Physics a-Materials Science & Processing,* vol. 79, pp. 1695-1709, Nov 2004.

[12] E. G. Gamaly*, et al.*, "Ablation of solids by femtosecond lasers: Ablation mechanism and ablation thresholds for metals and dielectrics," *Physics of Plasmas,* vol. 9, pp. 949-957, Mar 2002.

[13] D. J. Griffiths, "Electromagnetic Waves," in *Introduction to Electrodynamics*, 3 ed Upper Saddle River: Prentice-Hall, Inc., 1999, pp. 364-411.

[14] R. K. A. Miotello, "Mechanisms of Pulsed Laser Sputtering," in *Pulsed Laser Deposition of Thin Films*, a. G. K. H. Douglas B. Chrisey, Ed., ed New York: John Wiley & Sons, Inc., 1994, pp. 55-87.

[15] E. Vanderiet*, et al.*, "REDUCTION OF DROPLET EMISSION AND TARGET ROUGHENING IN LASER-ABLATION AND DEPOSITION OF METALS," *Journal of Applied Physics,* vol. 74, pp. 2008-2012, Aug 1993.

[16] B. X. Wu, "High-intensity nanosecond-pulsed laser-induced plasma in air, water, and vacuum: A comparative study of the early-stage evolution using a physics-based predictive model," *Applied Physics Letters,* vol. 93, Sep 2008.

[17] S. S. Mao*, et al.*, "Initiation of an early-stage plasma during picosecond laser ablation of solids," *Applied Physics Letters,* vol. 77, pp. 2464-2466, Oct 2000.

[18] S. Metev, "Process Characteristics and Film Properties in Pulsed Laser Deposition," in *Pulsed Laser Deposition of Thin Films*, a. G. K. H. Douglas B. Chrisey, Ed., ed New York: John Wiley & Sons, Inc., 1994, pp. 255-264.

[19] D. B. Geohegan, "Diagnostics and Characteristics of Pulsed Laser Deposition Laser Plasmas," in *Pulsed Laser Deposition of Thin Films*, a. G. K. H. Douglas B. Chrisey, Ed., ed New York: John Wiley & Sons, Inc., 1994, pp. 115-165.

[20] Y. Zhou*, et al.*, "Time-resolved observation of the plasma induced by laser metal ablation in air at atmospheric pressure," *Journal of Applied Physics,* vol. 108, Nov 2010.

[21] M. Von Allmen and A. Blatter, *Laser-beam interactions with materials : physical principles and applications*, 2nd updated ed. Berlin ; New York: Springer, 1995.

[22] D. H. A. B. Guus Rijnders, "Growth Kinetics During Pulsed Laser Deposition," in *Pulsed Laser Deposition of Thin Films: Applications-Led Growth of Functional Materials*, R. Eason, Ed., ed Hoboken: John Wiley & Sons, Inc., 2007, pp. 177-190.

[23] J. A. S. James S. Hotwitz, "Film Nucleation and Film Growth in Pulsed Laser Deposition of Ceramics," in *Pulsed Laser Deposition of Thin Films*, a. G. K. H. Douglas B. Chrisey, Ed., ed New York: John Wiley & Sons, Inc., 1994, pp. 229-254.

[24] Y. Maeno*, et al.*, "SUPERCONDUCTIVITY IN A LAYERED PEROVSKITE WITHOUT COPPER," *Nature,* vol. 372, pp. 532-534, Dec 1994.

[25] Z. Q. Mao*, et al.*, "Crystal growth of Sr2RuO4," *Materials Research Bulletin,* vol. 35, pp. 1813-1824, Aug 2000.

[26] S. Kittaka*, et al.*, "Higher-Tc superconducting phase in Sr2RuO4 induced by uniaxial pressure," *Physical Review B,* vol. 81, May 2010.

[27] Y. Maeno*, et al.*, "Enhancement of superconductivity of Sr2RuO4 to 3 K by embedded metallic microdomains," *Physical Review Letters,* vol. 81, pp. 3765-3768, Oct 1998.

[28] S. Madhavan*, et al.*, "Growth of epitaxial a-axis and c-axis oriented Sr2RuO4 films," *Applied Physics Letters,* vol. 68, pp. 559-561, Jan 1996.

[29] L. Walz and F. Lichtenberg, "REFINEMENT OF THE STRUCTURE OF SR2RUO4 WITH 100 AND 295 K X-RAY DATA," *Acta Crystallographica Section C-Crystal Structure Communications,* vol. 49, pp. 1268-1270, Jul 1993.

[30] Y. Maeno*, et al.*, "The intriguing superconductivity of strontium ruthenate," *Physics Today,* vol. 54, pp. 42-47, Jan 2001.

[31] F. Lichtenberg*, et al.*, "SR2RUO4 - A METALLIC SUBSTRATE FOR THE EPITAXIAL-GROWTH OF YBA2CU3O7-DELTA," *Applied Physics Letters,* vol. 60, pp. 1138-1140, Mar 1992.

[32] M. A. Zurbuchen*, et al.*, "Suppression of superconductivity by crystallographic defects in epitaxial Sr2RuO4 films," *Applied Physics Letters,* vol. 78, pp. 2351-2353, Apr 2001.

[33] Y. Krockenberger*, et al.*, "Growth of superconducting Sr2RuO4 thin films," *Applied Physics Letters,* vol. 97, Aug 2010.

[34] A. C. a. K. Hathaway, "Physics of Giant Magnetostriction," in *Handbook of Giant Magnetostrictive Materials*, G. Engdahl, Ed., ed San Diego, CA: Academic Press, 2000, pp. 1-48.

[35] I. ETREMA Products, "Data Sheet Terfenol-D ", Ames2011.

[36] D. McMasters, "Manufacture of TERFENOL-D," in *Handbook of Giant Magnetostrictive Materials*, G. Engdahl, Ed., ed San Diego, CA: Academic Press, 2000, pp. 95-98.

[37] G. E. a. C. B. Bright, "Device Application Examples," in *Handbook of Giant Magnetostrictive Materials*, G. Engdahl, Ed., ed San Diego, CA: Academic Press, 2000, pp. 287-322.

[38] F. Schatz*, et al.*, "MAGNETIC-ANISOTROPY AND GIANT MAGNETOSTRICTION OF AMORPHOUS TBDYFE FILMS," *Journal of Applied Physics,* vol. 76, pp. 5380-5382, Nov 1994.

[39] R. Osiander*, et al.*, "A microelectromechanical-based magnetostrictive magnetometer," *Applied Physics Letters,* vol. 69, pp. 2930-2931, Nov 1996.

[40] E. Quandt and K. Seemann, "Fabrication and simulation of magnetostrictive thin-film actuators," *Sensors and Actuators a-Physical,* vol. 50, pp. 105-109, Aug 1995.

[41] T. Honda*, et al.*, "FABRICATION OF MAGNETOSTRICTIVE ACTUATORS USING RARE-EARTH (TB,SM)-FE THIN-FILMS (INVITED)," *Journal of Applied Physics,* vol. 76, pp. 6994-6999, Nov 1994.

[42] A. Yourdkhani*, et al.*, "Magnetoelectric Perovskite-Spinel Bilayered Nanocomposites Synthesized by Liquid-Phase Deposition," *Chemistry of Materials,* vol. 22, pp. 6075-6084, Nov 2010.

[43] S. Xie*, et al.*, "Multiferroic CoFe2O4-Pb(Zr0.52Ti0.48)O3 core-shell nanofibers and their magnetoelectric coupling," *Nanoscale,* 2011.

Appendix A

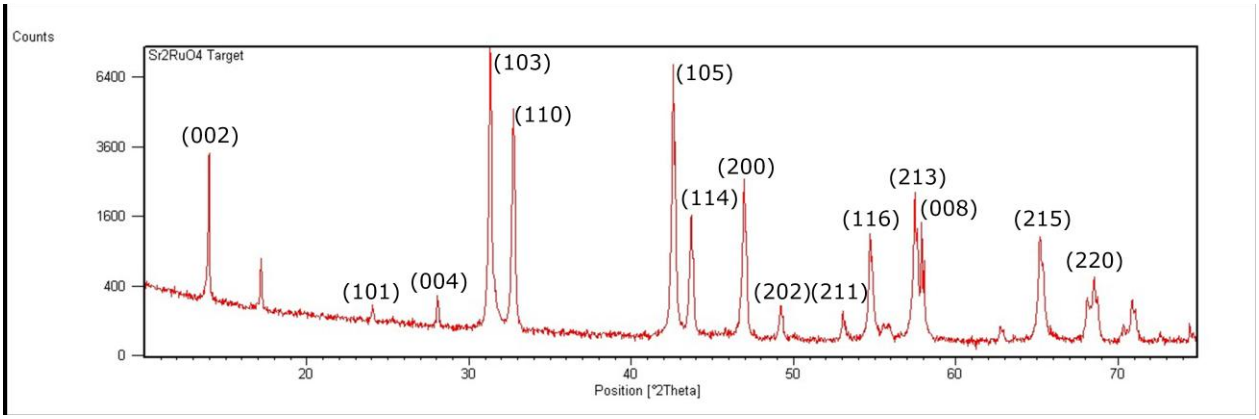

Figure A.1. Labeled θ-2θ XRD scan of Sr_2RuO_4 Target

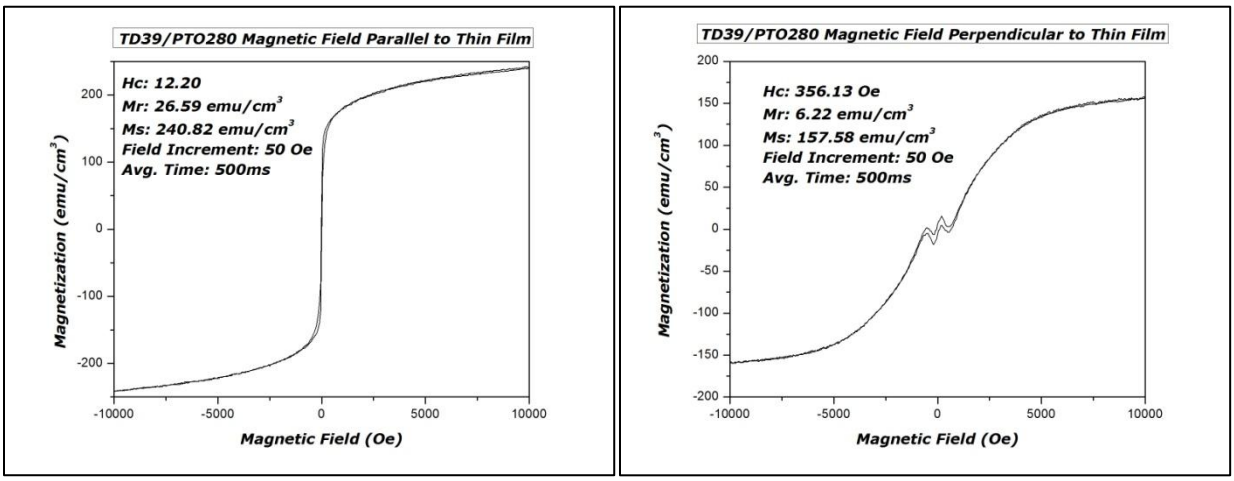

Figure A.2. AGM of TD39/PTO280

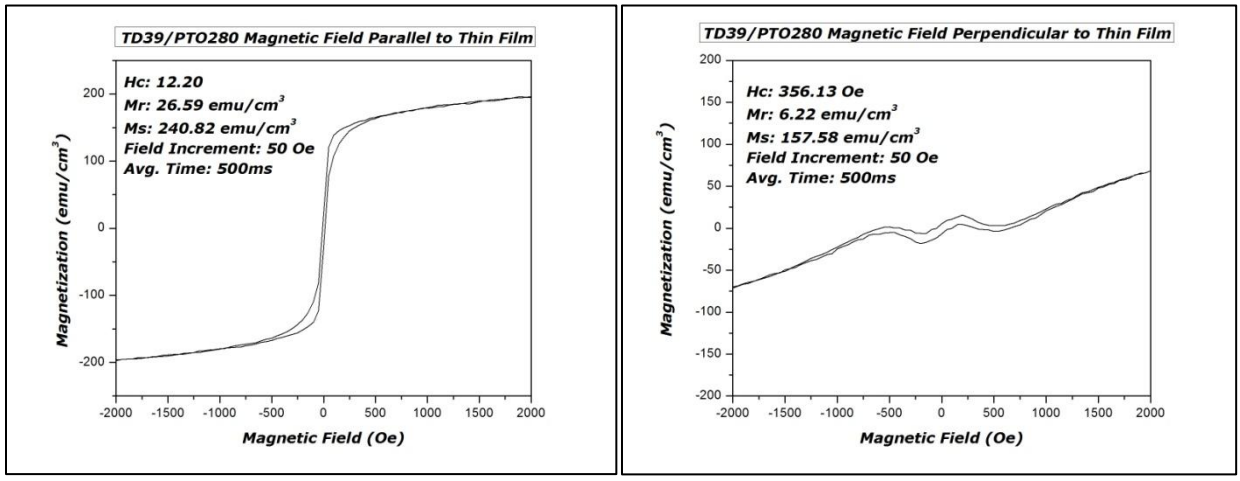

Figure A.3. AGM Expanded View of TD39/PTO280

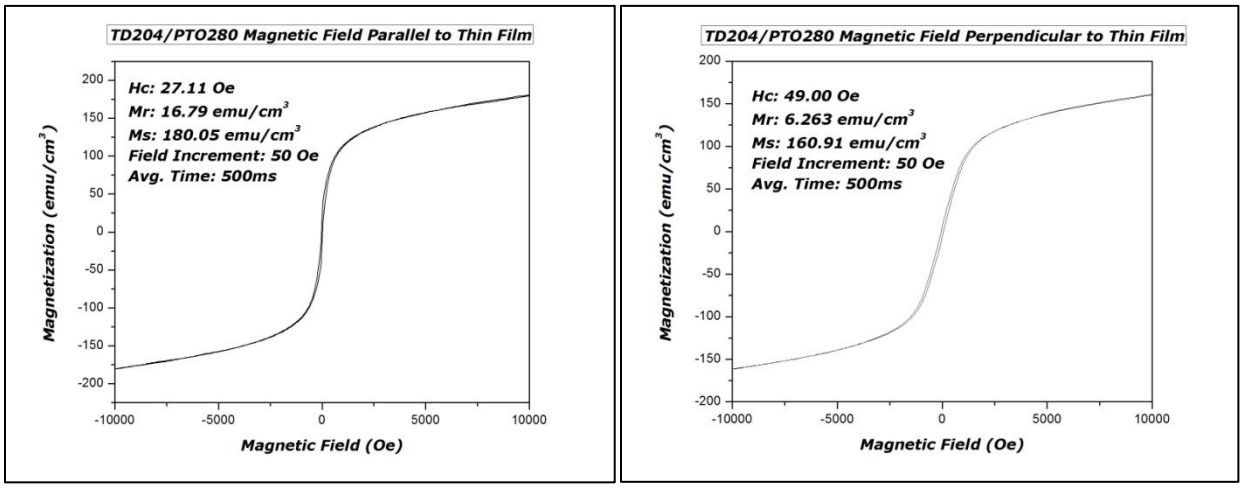

Figure A.4. AGM of TD204/PTO280

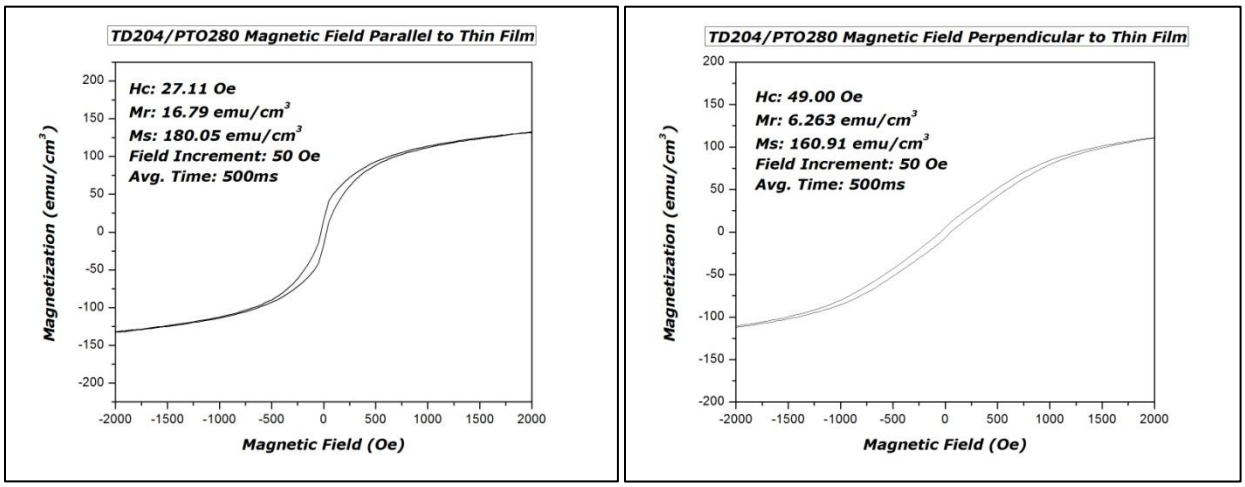

Figure A.5. AGM Expanded View of TD204/PTO280

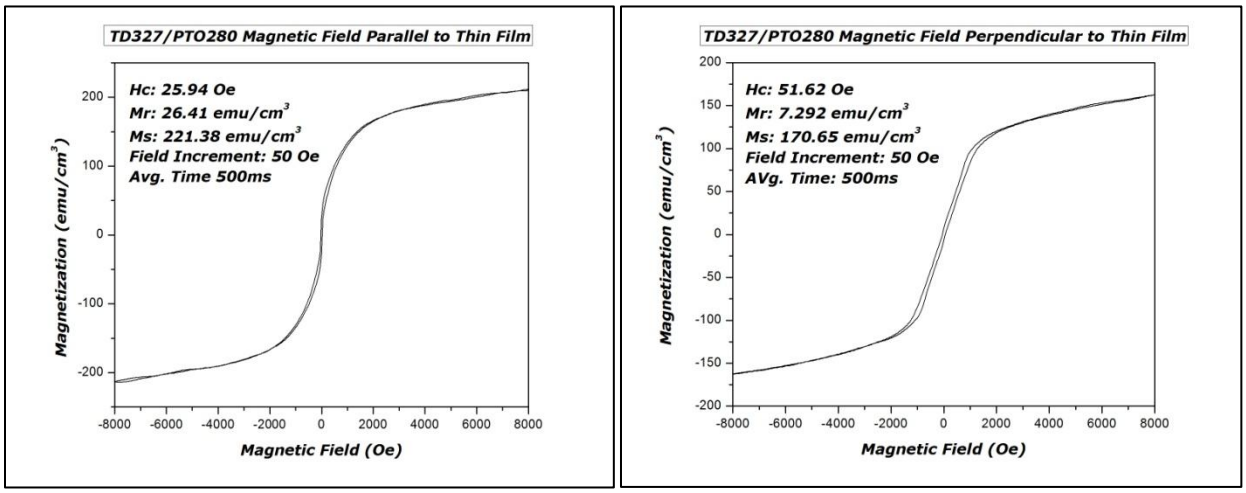

Figure A.6. AGM of TD327/PTO280

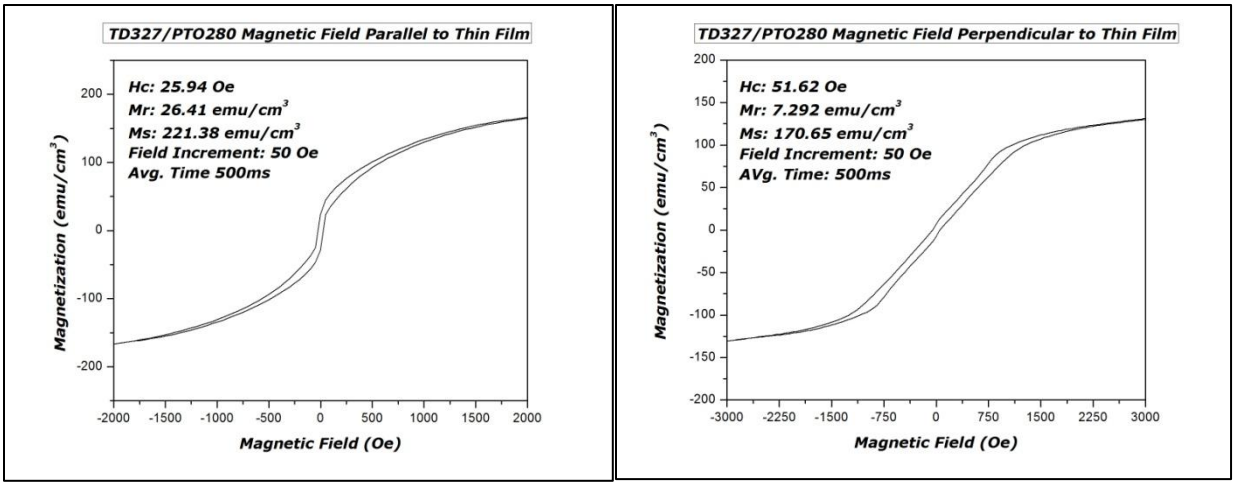

Figure A.7. AGM Expanded View of TD327/PTO280

Vita

Ezra Garza was born in January 3, 1984 in McAllen TX. In 2008 he graduated from the University of New Orleans with a Bachelor of Science in Physics. He will receive his Master of Science in Applied Physics from the University of New Orleans in August 2011.